DIPLOMARBEIT

Innovative Resonator Geometries for Enhanced Light Outcoupling in Terahertz Quantum Cascade Lasers

eingereicht von

Dominik Schock, BSc

an der

Technischen Universität Wien

Fakultät für Elektrotechnik und Informationstechnik

zum Zwecke der Erlangung des akademischen Grades

Diplom-Ingenieur

unter der Anleitung von

Projektass. Dipl.-Ing. Dr.rer.nat.
Michael Jaidl
Univ.Prof. Mag.rer.nat. Dr.rer.nat.
Karl Unterrainer

Wien, Jänner 2025

Acronyms

AM amplitude modulation

BTC bound-to-continuum

CSL chirped superlattice

cw continuous wave

DMWG double-metal waveguides

FEL Free Electron Laser

FM frequency modulation

FTIR Fourier transform infrared spectrometer

FWHM full width at half maximum

FWM four-wave mixing

GVD group velocity dispersion

HBVs Heterojunction Barrier Varactors

HEMTs High Electron Mobility Transistors

LIV light-current-voltage

LO longitudinal-optical

MBE molecular-beam epitaxy

NDR negative differential resistance

OCS carbonyl sulfide

PCB printed circuit board

PML perfectly matched layer

QCL Quantum Cascade Laser

QPML QCL-pumped molecular laser

RBF radial basis function

RF radio-frequency

RP resonant-phonon

SBDs Schottky Barrier Diodes

VEDs vacuum electronic devices

WGM whispering gallery modes

Glossary

COMSOL Multiphysics Simulation tool based on Finite-Elemente-Methode (FEM)

DTGS Deuterated Triglycine Sulfate (DTGS) is a form of TGS $(NH_2CH_2COOH)_3 \cdot H_2SO_4$ in which protons are replaced by deuterium. Due to its pyroelectric properties, it is commonly used in infrared spectroscopy and night vision applications.

globar A globar (portmanteau from glow and bar) is a radiation source for mid-infrared using joule heating, typically made from silicon carbide.

TPX Polymethylpentene (PMP), also known as TPX, is a thermoplastic polyolefin with the chemical structure poly(4-methyl-1-pentene) and transparent for terahertz radiation.

Abstract

Quantum Cascade Lasers are among the most promising candidates for closing the so-called THz gap. Using ring-shaped resonators, the generation of frequency combs along with high output power and compact device size has been successfully demonstrated [1]. The primary drawback is their radially symmetric radiation pattern, leading to a significant amount of unused light due to low collection efficiency.

The purpose of this thesis is to analyze different resonator geometries for enhanced light outcoupling. Instead of symmetric circular resonators, non-circular closed-loop resonators were tested to enhance the emission characteristics of these devices.

Two distinct geometries were simulated and fabricated: egg-shaped and pan-shaped resonators. These designs feature a minimum radius of curvature ranging from 350 μm to 100 μm.

To mitigate unwanted effects, Euler bends were implemented as connecting elements between circular sections, leading to a significant reduction of mode bouncing due to their linear change in curvature.

The devices demonstrated operation in both single-mode and multimode regimes. In the multimode regime, frequency comb formation was indicated by measuring the electrical beat note signal. In addition, by injection-locking the beating frequency to an external RF signal, the mode spacing could be modulated.

The far-field of the devices was characterized in terms of beam width, polarization, and direction of radiation. A specialized measurement setup was developed to enable far-field measurements from any direction.

Experimental results demonstrated a beam width of below 0.6 degrees at a distance of 20 cm, along with a strong rotational dependence of the far-field characteristics. Furthermore, the beam width was found to correlate with the direction of radiation.

Kurzfassung

Quantenkaskadenlaser gehören zu den vielversprechendsten Kandidaten, um die sogenannte THz-Lücke zu schließen. Durch den Einsatz von ringförmigen Resonatoren konnte die Erzeugung von Frequenzkämmen bei gleichzeitig hoher Ausgangsleistung und kompakter Größe erfolgreich demonstriert werden [1]. Der Hauptnachteil ist ihre radial symmetrische Abstrahlung, was zu einer erheblichen Menge ungenutzten Lichts aufgrund der niedrigen Lichtsammeleffizienz führt.
Ziel dieser Arbeit ist es, verschiedene Resonatorgeometrien zu untersuchen, die eine verbesserte Lichtauskopplung ermöglichen. Statt symmetrischer, ringförmiger Resonatoren wurden nicht-rotationssymmetrische, geschlossene Resonatoren entwickelt, um die Lichtemission zu optimieren. Es wurden zwei unterschiedliche Geometrien simuliert und gefertigt: eiförmige und pfannenförmige Resonatoren. Diese Designs weisen einen minimalen Krümmungsradius zwischen 350 μm und 100 μm auf.
Zur Reduktion unerwünschter Effekte wurden Euler-Bögen als Verbindungselemente zwischen den kreisförmigen Abschnitten eingesetzt. Dadurch konnte das Modebouncing durch die lineare Änderung der Krümmung signifikant verringert werden.
Die Laser konnten sowohl im Singlemode- als auch im Multimode-Regime betrieben werden. Im Multimode-Betrieb deutete die Messung des elektrischen Schwebungssignals auf die Bildung eines Frequenzkamms hin. Darüber hinaus konnte durch Injection-Locking der Schwebungsfrequenz an ein externes RF-Signal der Modenabstand moduliert werden.
Das Fernfeld der Laser wurde hinsichtlich Strahldurchmesser, Polarisation und Strahlrichtung charakterisiert. Ein spezieller Messaufbau wurde entwickelt, um Fernfeldmessungen aus jedem beliebigen Winkel zu ermöglichen.
Die experimentellen Ergebnisse zeigten eine Strahlbreite von unter 0,6 Grad bei einer Entfernung von 20 cm und eine starke Abhängigkeit der Fernfeldeigenschaften von der Drehung der Laser. Darüber hinaus wurde eine Korrelation zwischen Strahlbreite und Strahlrichtung gezeigt.

Contents

1 Introduction **8**

1.1 Generation of Terahertz Radiation . . . 8

2 Theory **12**

2.1 Quantum Cascade Laser . . . 12

2.1.1 Interband and Intersubband Transitions . . . 12

2.1.2 Active Region . . . 13

2.1.3 Optical Intersubband Transition . . . 15

2.2 Waveguides . . . 19

2.3 Resonators . . . 20

2.3.1 Euler Bends . . . 22

2.3.2 Dispersion . . . 25

2.3.3 Far-Field . . . 27

2.4 Frequency Comb . . . 28

2.4.1 Comb Formation . . . 28

2.4.2 Injection Locking . . . 30

3 Methods **31**

3.1 Design . . . 31

3.1.1 Size Optimization . . . 32

3.2 Simulation . . . 32

3.3 Processing of the Laser . . . 33

3.4 Measurement Setup . . . 34

3.4.1 Far-Field . . . 36

3.4.2 Submount . . . 39

4 Results **40**
4.1 Egg-shaped Resonators . . . 40
4.2 Pan-shaped Resonators . . . 41
4.3 Simulations . . . 41
4.4 Measurements . . . 46
4.4.1 LIV and spectral measurements . . . 46
4.4.2 RF Injection . . . 50
4.4.3 Far-Field Measurements . . . 52
4.4.4 Reflections . . . 52
4.4.5 Measurements . . . 52
4.4.6 Statistical Trends . . . 57

5 Discussion and Outlook **60**

Bibliography **62**

CHAPTER 1

Introduction

Terahertz radiation, commonly referred to as sub-millimeter waves, encompasses electromagnetic waves with frequencies ranging from 100 GHz to 30 THz, corresponding to wavelengths between 3 mm and 10 μm [2]. In the electromagnetic spectrum, terahertz radiation is situated within the transition region between microwave and infrared radiation, often associated with the far-infrared range. Oscillating circuits can reach frequencies up to about 300 GHz, though practical applications usually limit them to around 50 GHz, while conventional semiconductor lasers have a lower frequency limit of about 30 THz [3]. Consequently, the frequency range between these limits is commonly known as the "THz gap".
Even though generation and detection are challenging, there are many promising applications in the fields of sensing (material science, environmental monitoring, astronomy, security, biometrics, skin cancer diagnosis, explosives inspection) and telecommunications (wireless communication, high-speed data processing, satellite communication) [4].

1.1 Generation of Terahertz Radiation

Thermal Sources

The simplest THz sources are thermal sources. The peak radiation frequency of a black body can be easily calculated using Wien's displacement law. As shown in Figure 1.1, the peak radiation frequency of a black body at room temperature (293 K) is approximately 30 THz. By using Planck's law of blackbody radiation, the radiation spectrum can be calculated as shown in Figure 1.2. Although the peak radiation frequency is about 30 THz, the tail of the radiation extends down to below 10 THz.

Mercury lamps and globars can be utilized as basic radiation sources, although their peak radiation frequency is in the mid- to short-wavelength infrared, they also emit radiation extending into the terahertz range, as depicted in Figure 1.2 [5].
The spectral radiance in the terahertz region of a globar at 1650 K is significantly higher compared to that of a body at room temperature, assuming blackbody radiation (Figure 1.2). One downside is the frequency dependence on the spectral radiance as well as the limited power as Figure 1.2 illustrates.

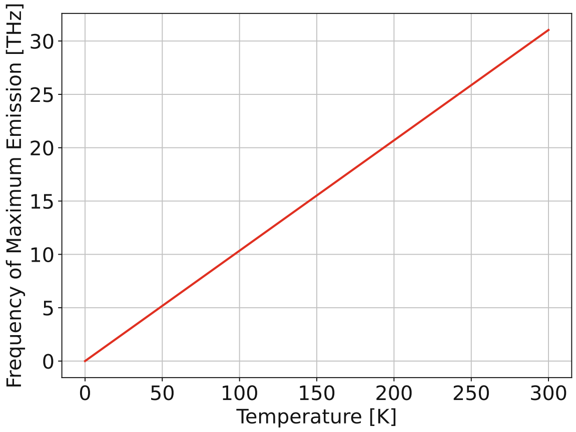

Figure 1.1: Wien's Displacement Law

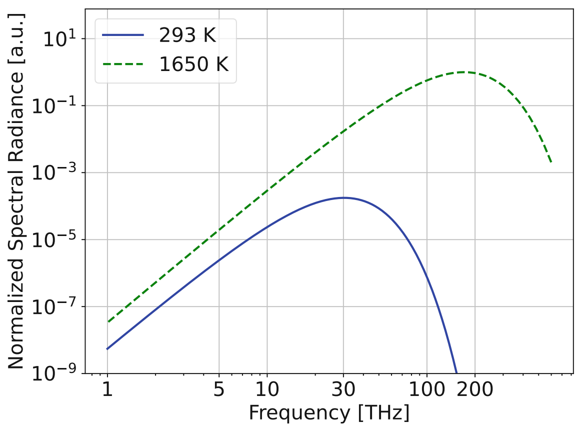

Figure 1.2: Black Body Spectrum

Vacuum Sources

In contrast to solid state electronic devices, in vacuum electronic devices (VEDs) the electron transport medium is vacuum and the transport is therefore ballistic [6]. Especially for high-power applications, VEDs exhibit superior properties due to ballistic transport in vacuum, compared to solid-state devices [6].
Typical VEDs are backward wave oscillators, gyrotrons, klystrons and traveling wave tubes [5]. Backward wave oscillators are one of the most established VEDs due to their high frequency tunability, stability, and high degree of monochromatic radiation, and are therefore used in spectroscopy [6, 7]. The main challenge is the fabrication and integration, due to the need for a three-dimensional vacuum-tight enclosure and an electron source [6, 8].

Solid State Sources

By pushing transistor technologies to their limits, it is possible to achieve frequencies of up to 1 THz using High Electron Mobility Transistors (HEMTs) [9, 10]. Another possibility is to use a nonlinear circuit to generate harmonics of the fundamental frequency. By applying a bandpass filter, a frequency multiplier can be realized.

For introducing this non-linearity, high-cutoff Schottky Barrier Diodes (SBDs), Heterojunction Barrier Varactors (HBVs) and High Electron Mobility Transistors (HEMTs) can be used [11–13]. The most promising devices are based on SBDs due to their high cutoff frequency, simple structure, room temperature operation, and high frequency and temperature stability [14, 15]. SBD-based devices operating at room temperature at frequencies up to 1.64 THz while maintaining an output power of 0.7 mW have been demonstrated [15]. The main limitations are the upper frequency limit, efficiency, power, and reliability [14].

Free Electron Laser (FEL)

Free Electron Lasers (FELs) are capable of delivering very high power, as well as high-frequency tunability [16]. Although several FELs operating in the THz region are available, they are not suitable for widespread or field use [2, 16].

Gas Lasers

By optically exciting the ro-vibrational transitions of gas molecules, it is possible to generate widely tunable terahertz radiation [17]. Various molecules can be used for generating THz radiation. A few examples include OCS, N_2O, CH_3F, HCN, and CO, all of which radiate around 1 THz [18]. Traditionally, CO_2 lasers have been used for pumping, but due to their large size (≈1 m) and the high voltage required, Quantum Cascade Laser (QCL) are increasingly replacing CO_2 lasers [18]. Recently, an N_2O QCL-pumped molecular laser (QPML) operating between 0.251 THz and 0.955 THz, with a spacing between the lasing transitions of 25.1 GHz, pumped by a QCL, was demonstrated [18]. Despite their wide tunability, molecular lasers still rely on discrete ro-vibrational transitions, making continuous frequency tuning impossible.

Photomixing Sources

By using two lasers, an optical beat frequency can be generated, defined as

$$\omega_{\text{beat}} = \omega_1 - \omega_2. \tag{1.1}$$

When a photoconductive switch, typically fabricated from GaAs, is illuminated with this beat note — provided the photon energy exceeds the semiconductor's bandgap and the carrier lifetime is sufficiently short — the switch's resistance is modulated at the beat frequency, thereby generating terahertz radiation [19].

Since the beat frequency depends only on the difference in frequency between the pump lasers, it is possible to tune the output frequency over a wide range with very high frequency stability, below 10 MHz [20, 21]. Currently, the highest frequency attainable using this technique is 5 THz [22].

Quantum Cascade Lasers

The idea of achieving gain in a semiconductor superlattice was first mentioned in 1971 [23]. Unlike an interband semiconductor laser, a Quantum Cascade Laser does not rely on the recombination of an electron from the conduction band with a hole from the valence band. Instead, a superlattice structure is used, allowing electrons to undergo intersubband transitions in the conduction band. The first operation in the THz range was reported in 2002 [24, 25].
QCLs are particularly compact and efficient sources for generating tunable and powerful terahertz radiation in the range of 1.2 to 5.4 THz [26, 27]. However, the main challenge remains achieving room temperature operation. Currently, the highest reported operating temperature is 261 K at around 4 THz [28].

CHAPTER 2

Theory

2.1 Quantum Cascade Laser

As mentioned in section 1.1, quantum cascade lasers (QCL) are among the most promising technologies for generating terahertz radiation. The purpose of this section is to provide a theoretical description of the working principles of a QCL.

2.1.1 Interband and Intersubband Transitions

Traditional semiconductor lasers utilize interband transitions, where an electron from the conduction band recombines with a hole in the valence band. As illustrated in Figure 2.1a), this leads to a non-discrete energy distribution governed by Fermi-Dirac statistics, resulting in a broadening of the optical transition energies. For energies higher than $E_{12} + E_{fe} + E_{fh}$ this even results in absorption.
In comparison, a Quantum Cascade Laser uses an intersubband transition in the conduction band, and therefore only involves electronic states. As a result, all transitions have nearly the same energy due to the similar curvature of both subbands, leading to a delta-like gain distribution (Figure 2.1b)). Another advantage of intersubband transitions is that the transition energy is not limited by the semiconductor band gap, allowing the transition energy to be tuned to smaller values by adjusting the width of the quantum wells which are formed by the thin layers of the semiconductor heterostructure.
Additionally, the carrier lifetime of intersubband transitions is in the range of picoseconds, whereas the carrier lifetime in interband transitions is in the range of nanoseconds [29–31]. In interband lasers, the recombination rate is dominated by radiative band-to-band transitions [32], while for intersubband transitions, fast non-radiative scattering processes

incorporating longitudinal-optical (LO) phonons are predominant [31].

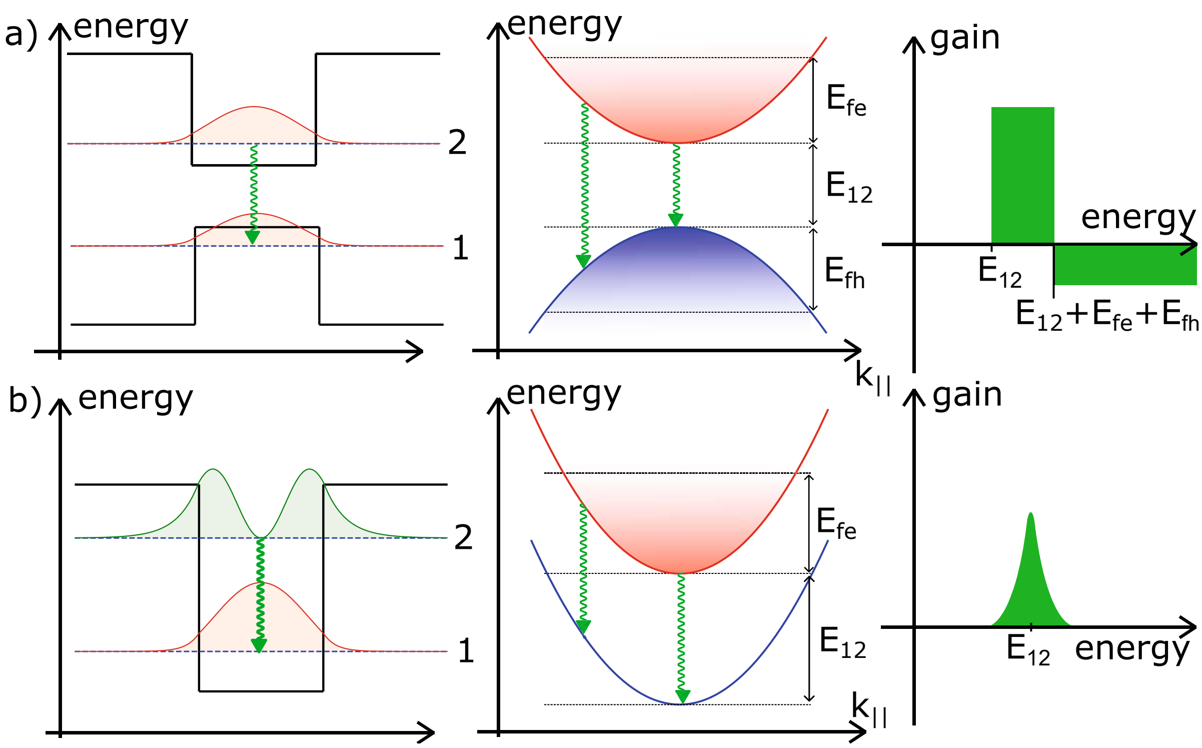

Figure 2.1: Comparison of interband and intersubband transition

2.1.2 Active Region

The active region of a QCL consists of a multi quantum well structure grown by molecular-beam epitaxy (MBE) in the III-V semiconductor material system. Figure 2.2 shows a schematic of two periods of the band diagram of the active region under an applied bias voltage. Each period comprises a gain region, where photons are generated, and an injection region.

There are mainly three different approaches for designing the active region.

Chirped Superlattice

The first THz QCLs were based on a chirped superlattice (CSL), where several quantum wells formed by the superlattice are coupled and form so-called minibands [33]. By placing two materials with a periodicity much larger than the lattice constant (approximately a factor of 10), an artificial crystal is formed, which splits the conduction and valence bands into multiple minibands [34].

Population inversion is achieved between the lowest state of the upper miniband and the highest state of the lower miniband, this occurs due to the strong coupling between the states within the miniband, thereby favoring intersubband scattering over interband scattering between the minibands [33].

Bound-to-Continuum

To improve the operating temperature and power performance, a so-called bound-to-continuum (BTC) structure with an isolated defect state inside the minigap can be used as the upper laser state instead of the miniband [33, 35]. The more diagonal transition reduces oscillator strength and non-radiative scattering processes, while improving injection efficiency and the upper-to-lower state lifetime ratio [33, 35, 36]. The miniband is utilized for an efficient depopulation of the lower lasing state [36].

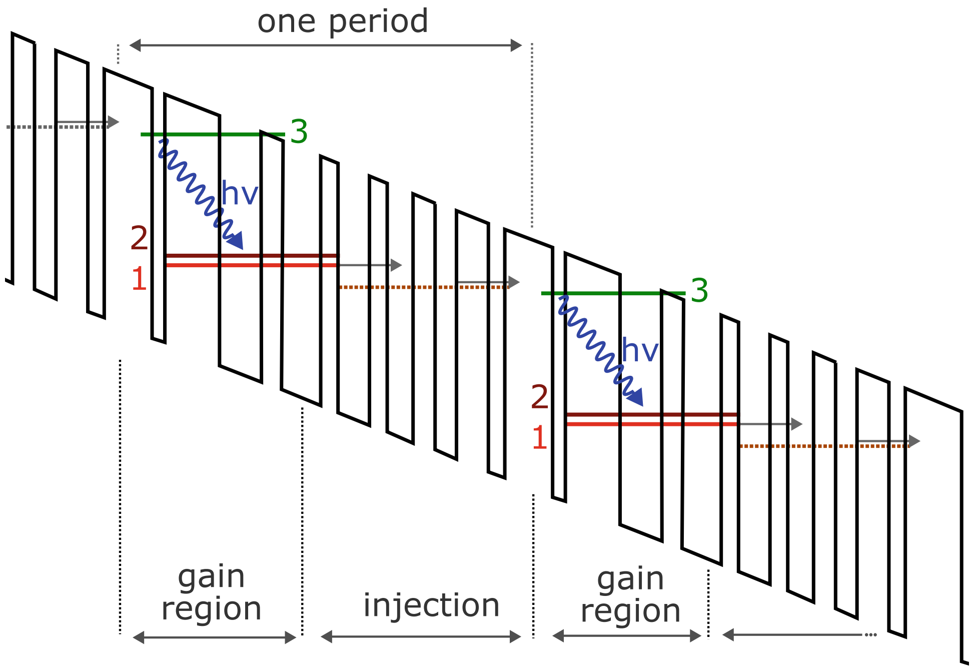

Figure 2.2: Illustration of the band diagram of two periods of a bound-to-continuum design of the active region of a QCL under bias voltage.

Resonant-Phonon

To further improve temperature performance, a resonant-phonon (RP) design can be used, where the lower lasing state is brought into resonance with the injector state (respectively the upper laser state), by matching the energy difference between the states to the LO-phonon energy ($\hbar\omega_{LO} \approx 36$ meV in GaAs) [35]. This results in very fast resonant LO-phonon transitions in the sub-picosecond range [33, 35, 37].

2.1.3 Optical Intersubband Transition

Every particle must obey the fundamental laws of energy and momentum conservation.

$$E(\mathbf{k}) - E(\mathbf{k}') = \hbar\omega, \quad \mathbf{k} - \mathbf{k}' = \mathbf{q} \approx 0 \tag{2.1}$$

In a perfect bulk crystal the electron can be assumed to be a free particle and therefore the energy can be expressed as

$$E(\mathbf{k}) = \frac{\hbar^2 \mathbf{k}^2}{2m^*}. \tag{2.2}$$

Because of the negligible momentum transfer of a photon during phototransitions, equation (2.2) cannot be fulfilled and therefore, no intersubband transition in a perfect bulk crystal without phonon interaction is possible [38].
For a semiconductor heterostructure, the dispersion relation can be written as

$$E_i(\mathbf{k}_{||}) = \epsilon_i \frac{\hbar^2 \mathbf{k}_{||}^2}{2m^*} \tag{2.3}$$

and the energy and momentum conservation laws can be expressed as

$$E_i(\mathbf{k}_{||}) - E_j(\mathbf{k}'_{||}) = \hbar\omega, \quad \mathbf{k}_{||} - \mathbf{k}'_{||} = \mathbf{q} \approx 0, \tag{2.4}$$

As a result if $\hbar\omega$ equals the intersubband energy difference $(\epsilon_i - \epsilon_j)$, the conditions (2.3) are fulfilled and an intersubband transition becomes possible [38].

The probability for an intersubband transition, triggered by an incident electromagnetic wave, can be calculated by assuming that the electric field of the wave is strong enough to alter the population of states but not to change the states themselves [39]. Therefore, the Hamiltonian can be split into two parts: an unperturbed Hamiltonian H_0 and the so-called interaction Hamiltonian H_{int}.

$$H = H_0 + H_{\text{int}} \tag{2.5}$$

The Hamiltonian of a charged electron with effective mass m^* and momentum $\mathbf{p}$ in a vector potential $\mathbf{A}$ can be expressed using the Coulomb gauge $\nabla \cdot \mathbf{A} = 0$ by

$$H = \frac{(\mathbf{p} - e\mathbf{A})^2}{2m^*}. \tag{2.6}$$

Assuming low intensity and therefore $|\mathbf{A}|^2 \ll 1$, we can write the Hamiltonian (2.6) as

$$H \approx \frac{\mathbf{p}^2}{2m^*} - \frac{e\,\mathbf{p}\cdot\mathbf{A}}{m^*} \tag{2.7a}$$
$$H_{\text{int}} = -\frac{e}{2m^*}\mathbf{A}\cdot\mathbf{p} \tag{2.7b}$$
$$H_0 = \frac{\mathbf{p}^2}{2m^*}. \tag{2.7c}$$

By assuming an incident planar electromagnetic wave with linear polarization $\boldsymbol{\varepsilon}$ and propagation vector $\mathbf{q}$

$$\mathbf{E} = E_0\boldsymbol{\varepsilon}\cos(\omega t - \mathbf{q}\cdot\mathbf{r}) \tag{2.8}$$

and using $\mathbf{E} = -\partial\mathbf{A}/\partial t$ along with the dipole approximation, one can derive

$$\mathbf{A} = -\frac{E_0}{2\omega}\boldsymbol{\varepsilon}\left(e^{i(\omega t-\mathbf{q}\cdot\mathbf{r})} - e^{-i(\omega t-\mathbf{q}\cdot\mathbf{r})}\right) \tag{2.9a}$$
$$H_{\text{int}}(t) = -\frac{e}{2m^*}\mathbf{A}\cdot\mathbf{p} = V\left(e^{i\omega t} - e^{-i\omega t}\right), \tag{2.9b}$$
$$V = \frac{eE_0}{2m^*\omega}\boldsymbol{\varepsilon}\cdot\mathbf{p} \tag{2.9c}$$

for the vector potential $\mathbf{A}$, the time dependent interaction Hamiltonian $H_{\text{int}}(t)$ as well as the time independent part V [40].

Transition Rate

The transition probability for an electron from state $|i\rangle$ with energy E_i to state $|f\rangle$ with energy E_f is defined by Fermi's golden rule:

$$W_{i\to f}(\hbar\omega) = \frac{2\pi}{\hbar}|\langle f|H_{\text{int}}|i\rangle|^2\delta(E_f - E_i \pm \hbar\omega) \tag{2.10}$$

By using the time-independent part of the interaction Hamiltonian (2.9c) we can rewrite equation (2.10) as

$$W_{i\to f}(\hbar\omega) = \frac{2\pi}{\hbar}\frac{e^2E_0^2}{4{m^*}^2\omega^2}|\langle f|\boldsymbol{\varepsilon}\cdot\mathbf{p}|i\rangle|^2\delta(E_f - E_i \pm \hbar\omega). \tag{2.11}$$

The delta function is only non-zero for two distinct cases: when $E_f = E_i + \hbar\omega$ a photon is absorbed and when $E_f = E_i - \hbar\omega$ a photon is emitted.

Due to interface roughness and phonon scattering, it is more accurate to use a Lorentzian function

$$\delta(E_f - E_i \pm \hbar\omega) \to \frac{\gamma/\pi}{(E_f - E_i \pm \hbar\omega)^2 + \gamma^2} \tag{2.12}$$

with half width γ instead of the delta function to account for line broadening [39]. Thus, the transition probability can be rewritten as:

$$W_{i\to f}(\hbar\omega) = \frac{2}{\hbar}\frac{e^2E_0^2}{4m^{*2}\omega^2}|\langle f|\boldsymbol{\varepsilon}\cdot\mathbf{p}|i\rangle|^2\frac{\gamma}{(E_f - E_i \pm \hbar\omega)^2 + \gamma^2}. \tag{2.13}$$

For a heterostructure, the wave functions can be expressed as

$$\psi_i(\mathbf{r}) = u_{\nu_i} f_i(\mathbf{r}), \tag{2.14a}$$

$$f_i(\mathbf{r}) = \frac{1}{\sqrt{S}} e^{i\mathbf{k}_{\perp i}\cdot\mathbf{r}_\perp}\chi_i(z) \tag{2.14b}$$

and the matrix element $\langle f|\boldsymbol{\varepsilon}\cdot\mathbf{p}|i\rangle$ for a heterostructure is given in equation (2.15) [40].

$$\begin{aligned}\langle f|\boldsymbol{\varepsilon}\cdot\mathbf{p}|i\rangle = \langle\chi_f|\chi_i\rangle\frac{1}{S}\int(\varepsilon_x p_x + \varepsilon_y p_y)\, e^{-i\mathbf{k}_{\perp f}\cdot\mathbf{r}_\perp}e^{-i\mathbf{k}_{\perp i}\cdot\mathbf{r}_\perp}\,dx\,dy \\ + \delta(\mathbf{k}_{\perp f} - \mathbf{k}_{\perp i})\varepsilon_z\langle\chi_f|p_z|\chi_i\rangle\end{aligned} \tag{2.15}$$

The term $\langle\chi_f|\chi_i\rangle$ is only non-zero for $f = i$ due to the orthogonality of different subbands [38]. This leads to the very important result that only light polarized parallel to the growth direction can couple and therefore introduce a photo transition.

By using the relation $[z, p_z] = i\hbar$ and the commutator between the displacement operator and the Hamiltonian, $[H_0, z]$, where $H_0 = \frac{p^2}{2m} + V(r)$, one can derive a relation between the momentum and position matrix elements.

$$[H_0, z] = \left[\frac{p^2}{2m} + V(r), z\right] \tag{2.16a}$$

$$= \frac{1}{2m}[p^2, z] \tag{2.16b}$$

$$= \frac{1}{2m}\left(p[p, z] + [p, z]p\right) \tag{2.16c}$$

$$= \frac{\hbar}{im}p. \tag{2.16d}$$

$$\langle x_n|[H_0, z]|x_m\rangle = \langle x_n|H_0 z|x_m\rangle - \langle x_n|zH_0|x_m\rangle \tag{2.16e}$$

$$= \langle x_n|E_n z|x_m\rangle - \langle x_n|zE_m|x_m\rangle \tag{2.16f}$$

$$= (E_n - E_m)\langle x_n|z|x_m\rangle. \tag{2.16g}$$

$$\frac{\hbar}{im}\langle x_n|p|x_m\rangle = (E_n - E_m)\langle x_n|z|x_m\rangle \tag{2.16h}$$

$$\langle x_n|p|x_m\rangle = im\omega_{nm}\langle x_n|z|x_m\rangle. \tag{2.16i}$$

This leads to the more familiar notation in the **r**-representation [39, 40].

By using equations (2.13), (2.15), and (2.16i), we obtain

$$W_{i\to f}(\hbar\omega) = \frac{e^2E_0^2}{2\hbar}|\langle\chi_f|z|\chi_i\rangle|^2\frac{\gamma}{(E_f - E_i \pm \hbar\omega)^2 + \gamma^2} \tag{2.17}$$

for a wave polarized parallel to the growth direction z. If the photon energy equals the energy between two adjacent states ($\hbar\omega = \pm(E_f - E_i)$), the transition rate is maximized. Therefore, the maximum stimulated emission rate can be expressed as

$$W_{i\to f}(\hbar\omega) = \frac{e^2E_0^2}{2\hbar\gamma}|\langle\chi_f|z|\chi_i\rangle|^2. \tag{2.18}$$

Optical Gain

To calculate the optical gain, a plane wave with power density

$$P = \frac{1}{2}\varepsilon_0 ncE_0^2 \tag{2.19}$$

and photon flux

$$\phi = \frac{1}{2}\left(\frac{\varepsilon_0 ncE_0^2}{\hbar\omega}\right)\omega L_p \tag{2.20}$$

is considered, where L_p is the period length of the active region, c the vacuum speed of light, ε_0 the vacuum permittivity, n the refractive index, E_0 the amplitude of the electric field and ω the angular frequency [40].

The optical gain is defined as

$$G = \frac{d\phi/dy}{\phi} \tag{2.21}$$

with

$$d\phi = W_{\text{fi}}^{\text{max}}n_f w dy - W_{\text{fi}}^{\text{max}}n_2\omega dy, \tag{2.22}$$

denoting the change in photon flux in a waveguide with width w over a distance dy [40].

By using equations (2.20), (2.22), and (2.18), one can derive:

$$g(\omega)_{\text{max}} = \frac{2\pi e^2|\langle\chi_f|z|\chi_i\rangle|^2(n_i - n_f)}{\varepsilon_0 n_{\text{refr}}\lambda L_p\gamma} \tag{2.23}$$

with n_i and n_f denoting the population per unit area of the initial and final state, λ

representing the wavelength, e the electron charge, and n_{refr} the refractive index.

An important quantity is the so-called peak gain cross section, which can be calculated as depicted in formula (2.24) [39].

$$g_c = \frac{g_{\max}}{n_f - n_i} \tag{2.24}$$

Commonly, the oscillator strength (equation (2.25)) is used instead of the matrix element.

$$f_{fi} = \frac{2m_0\omega}{\hbar} |\langle \chi_f | z | \chi_i \rangle|^2 \tag{2.25}$$

Therefore, the peak gain cross section can be expressed as:

$$g_c = \frac{\pi e^2 \hbar f_{fi}}{\varepsilon_0 n_{\text{refr}} \lambda L_p \gamma m_0 \omega} \tag{2.26}$$

with m_0 denoting the electron mass.

2.2 Waveguides

In principle, there are two different approaches for a THz waveguide. The so-called single plasmon waveguide consists of a metal layer on the top and a thin, highly doped GaAs layer on the bottom as a plasmon layer [39]. The main disadvantage of this structure is its very low overlap factor (equation (2.27)), in the range of $\Gamma = 0.1 - 0.5$, which also limits the minimum width of the waveguides to about 100 μm [33]. The resulting large mode size offers the advantages of a less divergent beam and a more favorable ratio of mirror losses to waveguide losses, leading to high efficiency and output power [33].

More commonly used are the so-called double-metal waveguides (DMWG). Instead of the plasmon layer, a metal layer is used on the bottom side of the active region, thereby drastically improving the overlap factor ($\Gamma \approx 1$) as well as the temperature performance [41–43]. The downside is the large impedance mismatch between the guided mode and the free-space propagation, which results in poor far-field properties [39].

$$\Gamma = \frac{\int_{\text{active region}} \mathrm{d}z\, \mathrm{d}x\, E_z^2(z,x)\varepsilon(x,z)}{\int_{-\infty}^{\infty} \mathrm{d}z\, \mathrm{d}x\, E^2(z,x)\varepsilon(x,z)} \tag{2.27}$$

2.3 Resonators

The simplest resonator is the Fabry-Pérot resonator, which has a rectangular shape and, for terahertz radiation, typically has a width in the μm range and a length in the mm range. The interface between air and GaAs acts as a mirror, allowing standing waves to form with a frequency spacing of

$$\Delta f = \frac{c}{2nL} \tag{2.28}$$

where L denotes the length of the resonator, c is the vacuum speed of light, and n is the refractive index. For improved performance, the ends (facets) of the resonator can be cleaved rather than etched, making them atomically flat.

Another approach involves ring-shaped resonators, which support whispering gallery modes (WGM). These modes were originally discovered in the cathedral of St. Paul for sound waves and described by Lord Rayleigh [44]. Due to continuous total internal reflection, light is guided along the outer perimeter of the cavity, creating very strong resonances [45]. The significant advantage of these WGM is their very high Q-factor [46, 47].
Another advantage is the overall small size of the cavities, which also do not require any facets [48].

The mode spacing can be calculated similarly to that of a Fabry-Pérot resonator

$$\Delta f = \frac{c}{2nr\pi} \tag{2.29}$$

where r is the outer radius of the ring.

The outcoupling of light is due to processing imperfections such as sidewall roughness as well as the evanescent field, which extends outside the ring.
The outcoupling caused by the evanescent field can be calculated as demonstrated in [49]. The electric field inside a slab waveguide that is bent into a ring shape is given by

$$\Psi_g = A\cos(\kappa\hat{x})e^{-\beta R\phi}, \tag{2.30}$$

where β is the propagation constant, $\hat{x}$ is the coordinate in the direction of the waveguide, and κ is defined as

$$\kappa = \sqrt{n_c^2k^2 - \beta^2} \tag{2.31}$$

with n_c representing the refractive index of the waveguide, and k denoting the free-space

wavenumber.
By extending the two-dimensional diffraction integral, one can derive the following equation for the field outside the waveguide:

$$\Psi_r(r') = \frac{iR}{4}\int_{-\pi/2}^{\pi/2}\left(\Psi_g(w)\frac{\partial H_0^{(2)}(nk\rho)}{\partial r} - H_0^{(2)}(nk\rho)\frac{\partial \Psi_g(w)}{\partial r}\right)d\Phi, \tag{2.32}$$

with n being the refractive index of the surrounding medium and R the middle radius of the waveguide.
By using the large-argument approximation for the Hankel function $H_0^{(2)}(nk\rho)$ at very large distances ρ, as well as the method of steepest descent, one can solve the integral (2.32) and obtain formula (2.34) for the far-field. With γ defined as

$$\gamma = \sqrt{\beta^2 - n^2k^2}. \tag{2.33}$$

$$\Psi_r(r') = iA\sqrt{\frac{R}{nk\gamma r'}}\frac{\kappa\gamma}{\sqrt{\kappa^2+\gamma^2}}e^{-\frac{\gamma^3}{3\beta^2}R}e^{i\left(\frac{\beta R}{2}-nkr'\right)} \tag{2.34}$$

With the definition of the power attenuation coefficient per unit length, where ΔP_r is the total radial power outflow, and P_g is the total power carried by the guided mode:

$$\alpha = \frac{\Delta P_r}{2\pi R P_g} \tag{2.35}$$

and

$$\Delta P_r = 4\pi r' nk|\Psi_r|^2 \tag{2.36a}$$

$$P_g = \frac{2|A|^2\beta}{\gamma(1+\gamma d)} \tag{2.36b}$$

we can then derive the following equation:

$$\alpha = \frac{\kappa^2\gamma^2 e^{\gamma w}}{\beta\left(1+\frac{1}{2}\gamma w\right)(\kappa^2+\gamma^2)}e^{-\frac{2\gamma^3}{3\beta^2}R} \tag{2.37}$$

Therefore, the radiative power should increase exponentially with increasing radius R as well as with increasing width of the laser w.

Figure 2.3 shows the simulated mode profile for two ring lasers.
It is clearly visible that the mode extends further out for the ring with a smaller radius. By simulating the far-field of the ring, the impact of both the radius and the width of the waveguide on the radiated power can be calculated.
Figure 2.4 shows the power attenuation coefficient in dB, as defined previously, for both

the simulation and the analytical calculation.

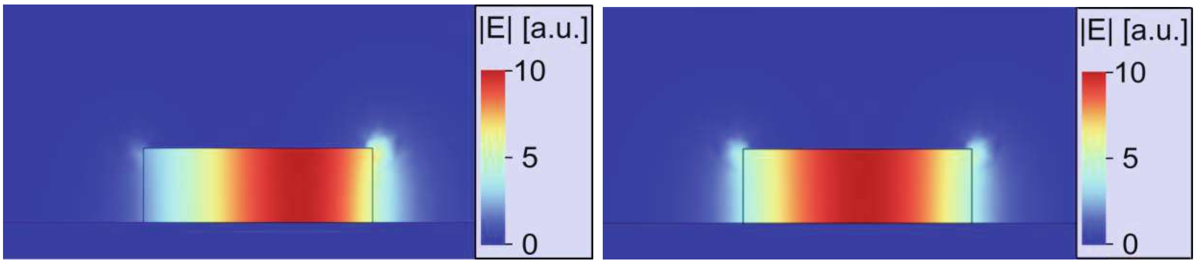

(a) Radius: 222 μm (b) Radius: 1978 μm

Figure 2.3: Comparison of the absolute value of the electric field of mode profile of a double-metal ring laser with a height of 13 μm and a width of 45 μm at 2.4 THz. The top of the waveguide as well as the bottom plane are assumed to be ideal electrical conductors, and the GaAs laser is surrounded by vacuum.

Although for very small radii the simulation and the calculation seem to match, for larger radii the calculation clearly underestimates the radiated power. This discrepancy is most likely due to the number of approximations used in the analytical formula (2.37). For example, the field is assumed to be invariant in the z-direction, which, as the simulation shows, does not hold outside the waveguide, especially for a waveguide with very small height, like the one simulated.

According to equation (2.37), the far-field intensity should increase exponentially with increasing width of the waveguide.
However, the simulation reveals a much more complex behavior. As shown in Figure 2.5, the radiated power decreases exponentially for small radii until it reaches approximately 35 μm, which is close to the wavelength at 2.4 THz in GaAs (34.6 μm). Between 35 μm and 45 μm, α remains relatively constant, and for larger widths, it increases exponentially, which aligns with equation (2.37).

2.3.1 Euler Bends

As shown earlier, the radius of the waveguide has a significant impact on the radiative power of the far-field. Therefore, by varying the radius, the radiated power should also vary. To minimize losses as well as other effects, such as mode bouncing, it is necessary to change the radius as smoothly as possible.
One common approach is to use Euler bends instead of abrupt changes in curvature. Euler bends have the unique property of changing the radius of a curve linearly with the curve length [50, 51].

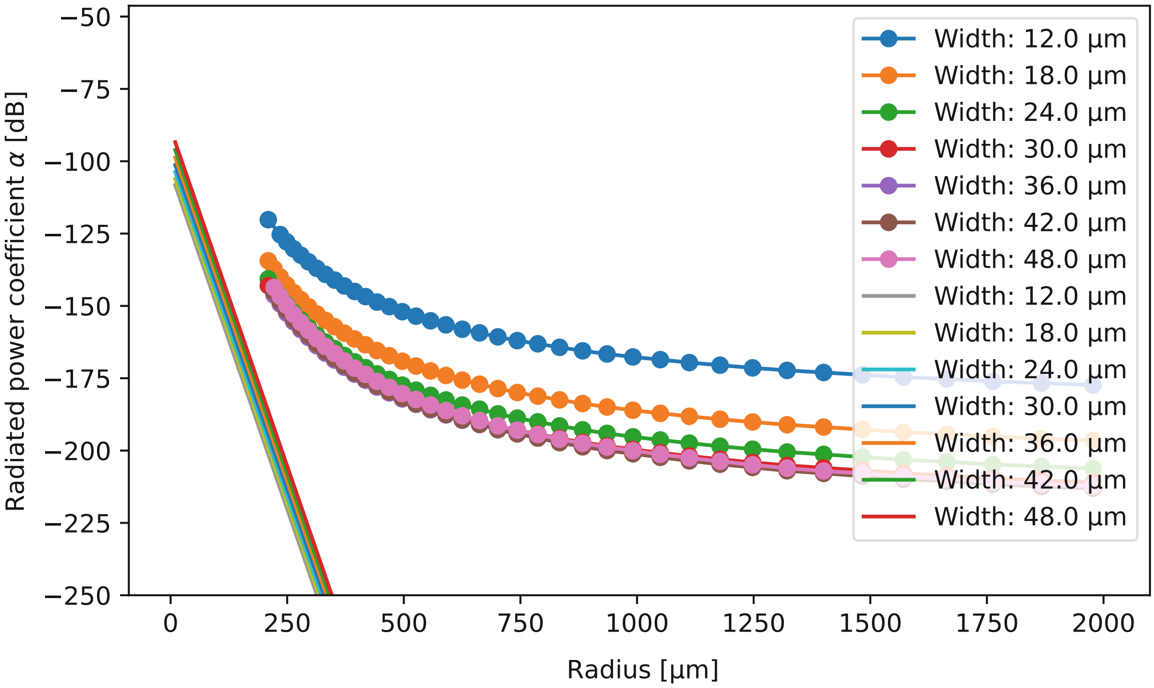

Figure 2.4: Radiated power coefficient of a ring laser at 2.4 THz with a height of 13 μm and different widths plotted over the outer radius of the ring. The solid lines represent the calculated values, while the lines with circular markers represent the simulated ones.

The curvature with radius R, and ϕ being the angle between the tangent of the initial point and the final point of a curve section with length s is defined as

$$\frac{1}{R} = \frac{d\phi}{ds} \propto s, \tag{2.38}$$

which by definition has to be proportional to the length of the curve.
Therefore, we can write

$$Rs = \text{const} = R_c s_0, \tag{2.39a}$$

$$R = \frac{R_c s_0}{s} \tag{2.39b}$$

with R_c being the radius at the end of the curve with length s_0. Using equation (2.38), we get

$$\frac{ds}{d\phi} = \frac{R_c s_0}{s}, \tag{2.40a}$$

$$ds \cdot s = R_c s_0 \, d\phi, \tag{2.40b}$$

$$s = \sqrt{2 R_c s_0 \phi}. \tag{2.40c}$$

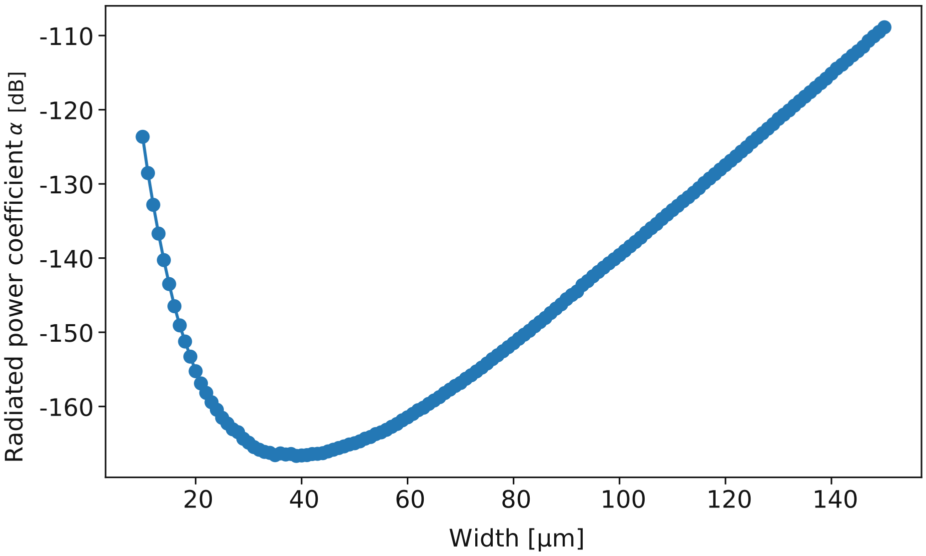

Figure 2.5: Radiated power coefficient of a ring laser at 2.4 THz with a height of 13 μm and an outer radius of 1000 μm, considering material dispersion as defined in Equation 2.45, plotted as a function of the ring width.

Because $x = x(s(\phi))$, we can use the chain rule of calculus

$$\frac{dx}{d\phi} = \frac{dx}{ds} \cdot \frac{ds}{d\phi}. \tag{2.41}$$

With figure 2.6, it is straightforward to derive the relation

$$\frac{dx}{ds} = \cos(\phi). \tag{2.42}$$

Putting everything together, we get:

$$\frac{dx}{d\phi} = \frac{\sqrt{R_c s_0}}{\sqrt{2\phi}} \cos(\phi). \tag{2.43}$$

By performing the same calculation for the y-coordinate, we arrive at the equations for the x and y coordinates, which are also known as Fresnel integrals:

$$x = \int_0^\phi \frac{\sqrt{R_c s_0}}{\sqrt{2t}} \cos(t)\, dt, \tag{2.44a}$$

$$y = \int_0^\phi \frac{\sqrt{R_c s_0}}{\sqrt{2t}} \sin(t)\, dt. \tag{2.44b}$$

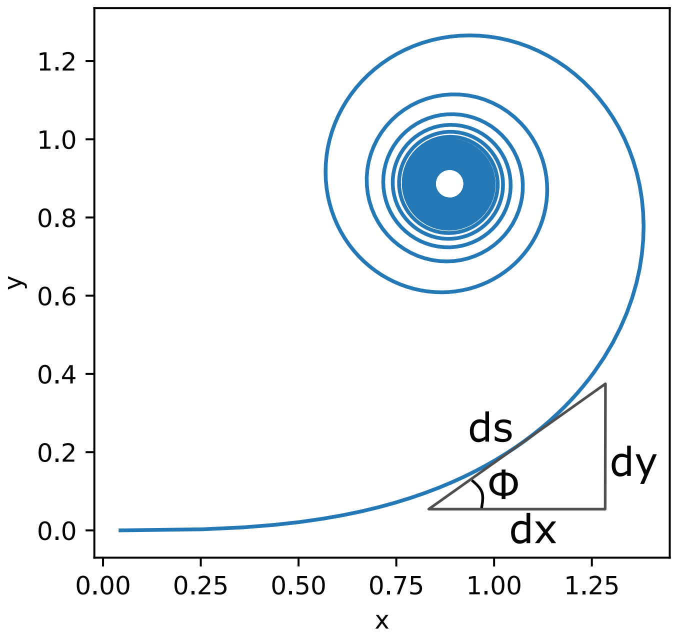

Figure 2.6: Euler spiral with $R_c = 1$ and $s_0 = 1$

2.3.2 Dispersion

The dispersion is a crucial parameter, especially in the context of frequency comb formation. The main contributors to the dispersion are material dispersion, waveguide dispersion, and gain-induced dispersion, with material dispersion dominating, especially near the Reststrahlen band [52].

Material Dispersion

Near the Reststrahlen band, the refractive index strongly depends on the frequency. For GaAs/AlGaAs, which is the dominant material system for THz QCLs, this can be described by a damped harmonic oscillator model [53]:

$$\varepsilon(\omega) = \varepsilon_\infty \left(1 + \frac{\omega_{\mathrm{LO}}^2 - \omega_{\mathrm{TO}}^2}{\omega_{\mathrm{TO}}^2 - \omega^2 - i\omega\gamma_{\mathrm{PH}}}\right) \tag{2.45}$$

where $\varepsilon_\infty = 10.89$ is the high-frequency dielectric constant, $\omega_{\mathrm{TO}} = 8.06\,\mathrm{THz}$ is the transverse-optical (TO) phonon frequency, $\omega_{\mathrm{LO}} = 8.76\,\mathrm{THz}$ is the longitudinal-optical (LO) phonon frequency, and $\gamma_{\mathrm{PH}} = 72.5 \times 10^{10}\,\mathrm{s}^{-1}$ is the phonon damping constant. Figure 2.7 illustrates the dielectric function of GaAs, including the TO phonon frequency and the LO phonon frequency.

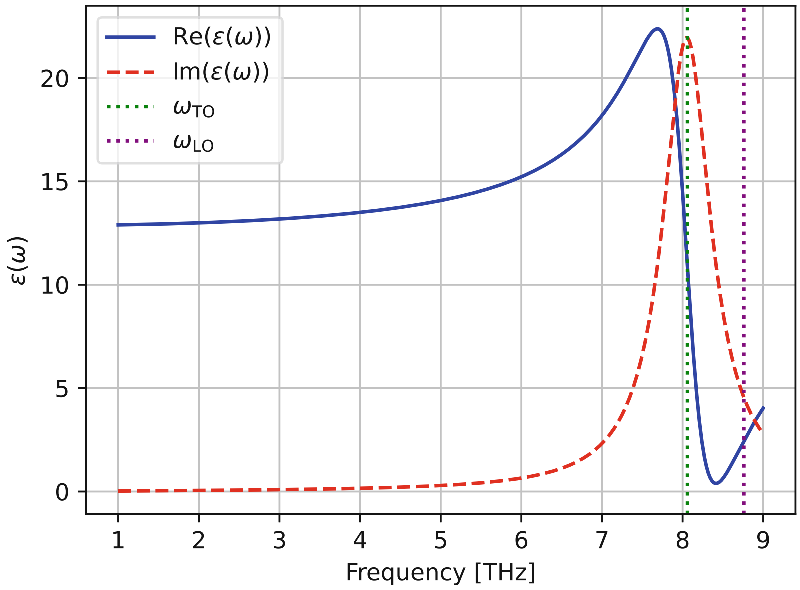

Figure 2.7: Dielectric function according to equation (2.45) for GaAs

GVD

One commonly used parameter for the dispersion is the group velocity dispersion (GVD), which is defined as

$$\text{GVD} = \frac{\partial}{\partial \omega}\left(\frac{1}{v_g}\right). \tag{2.46}$$

By using the expressions

$$k = \frac{\omega n}{c}, \tag{2.47a}$$

$$dk = \frac{1}{c}\left(n(\omega) + \omega\frac{\partial}{\partial \omega}n(\omega)\right) d\omega \tag{2.47b}$$

and the definition of the group velocity, we can derive the following relation between the group velocity and the group refractive index:

$$v_g = \frac{\partial \omega}{\partial g} = \frac{c}{n + \omega\frac{\partial n}{\partial \omega}} = \frac{c}{n_g} \tag{2.48}$$

Therefore we can rewrite the group velocity dispersion as

$$\text{GVD} = \frac{\partial}{\partial \omega}\left(\frac{n_g}{c}\right). \tag{2.49}$$

2.3.3 Far-Field

The far-field can be described using Fourier optics, which models the propagating wave as a superposition of plane waves.
If the amplitude distribution at one point is known, it can be calculated for any arbitrary point in space by multiplying the Fourier transform of the amplitude distribution, $A_{k_x,k_y}(z)$, with the transfer function of the system, $H(k_x, k_y; z)$:

$$A_{k_x,k_y}(z) = H(k_x, k_y; z)A_{k_x,k_y}(0) \tag{2.50}$$

The transfer function of free space can be expressed as

$$H(k_x, k_y; z) = e^{-j\sqrt{k^2-k_x^2-k_y^2}z} \approx e^{j\frac{k_x^2+k_y^2}{2k}z}e^{-jkz} \tag{2.51}$$

by assuming paraxial wave vectors [54].

Therefore, we can calculate the output signal using a two-dimensional convolution:

$$\begin{aligned} a_{\text{out}}(x, y; z) &= \mathcal{F}^{-1}\left\{H(k_x, k_y; z)A_{k_x,k_y}(0)\right\} \\ &= a_{\text{in}} * h \\ &= \iint_{-\infty}^{\infty} h(x - x', y - y')a_{\text{in}}(x', y')\, dx'\, dy' \end{aligned} \tag{2.52}$$

with

$$h(x, y) = \mathcal{F}^{-1}\left\{H(k_x, k_y; z)\right\} = h_0\, e^{-jk\frac{x^2+y^2}{2z}} \tag{2.53}$$

which results in [54]:

$$a_{\text{out}}(x, y; z) = e^{-jk\frac{x^2+y^2}{2z}} \iint_{-\infty}^{\infty} e^{-jk\frac{x'^2+y'^2}{2z}} a_{\text{in}}(x', y')e^{-jk\frac{xx'+yy'}{z}}\, dx'\, dy' \tag{2.54}$$

For the far-field, it is assumed that $k(x'^2 + y'^2)/(2z) \ll 1$, and therefore

$$\frac{x'^2 + y'^2}{\lambda d} \ll 1 \tag{2.55}$$

where d is the distance from the source. Condition (2.55) is also called the *Fraunhofer condition*.

Thus, the far-field can be calculated as

$$a_{\text{out}}(x, y; z) = e^{-jk\frac{x^2+y^2}{2z}} \iint_{-\infty}^{\infty} a_{\text{in}}(x', y')e^{-jk\frac{xx'+yy'}{z}}\, dx'\, dy'. \tag{2.56}$$

Stratton-Chu Formula

For numerical solutions, the Stratton-Chu formula can be implemented to calculate the far-field from the near-field, with equation 2.57a for the 3D case and (2.57b) for the 2D case [55–57]:

$$\mathbf{E}_p = \frac{jk}{4\pi}\mathbf{r}_0 \times \int \left[\mathbf{n} \times \mathbf{E} - \eta\, \mathbf{r}_0 \times (\mathbf{n} \times \mathbf{H})\right] e^{jk\mathbf{r}\cdot\mathbf{r}_0}\, dS \tag{2.57a}$$

$$\mathbf{E}_p = \frac{\sqrt{\lambda} jk}{4\pi}\mathbf{r}_0 \times \int \left[\mathbf{n} \times \mathbf{E} - \eta\, \mathbf{r}_0 \times (\mathbf{n} \times \mathbf{H})\right] e^{jk\mathbf{r}\cdot\mathbf{r}_0}\, dS \tag{2.57b}$$

This approach is used in finite element simulation tools like COMSOL Multiphysics [55].

2.4 Frequency Comb

A frequency comb is a superposition of phase-coherent cavity modes that are equally spaced in the frequency domain and therefore capable of producing very short laser pulses in the time domain [58, 59].

To generate short pulses (amplitude modulation (AM)), the phase between the modes has to be not only constant but zero. This is for QCL typically not the case and leads to the possibility of the formation of a frequency-modulated (FM) comb, which exhibits constant output power [60, 61].

The frequencies of the comb lines f_n are given by

$$f_n = f_0 + n f_r \tag{2.58}$$

with f_0 denoting the carrier offset frequency and the mode spacing f_r, which is equal to the repetition rate of the laser (Figure 2.8). If the comb spans an octave in frequency, the carrier offset frequency can be measured by using second harmonic generation [62]:

$$2f_n - f_{2n} = 2(n f_{\text{rep}} + f_{\text{ceo}}) - (2n f_{\text{rep}} + f_{\text{ceo}}) = f_{\text{ceo}} \tag{2.59}$$

Therefore, the frequency of each comb line can be linked to the repetition rate f_{rep} and enables the use in applications like spectroscopy and time metrology [60].

2.4.1 Comb Formation

In principle, there are two ways to achieve frequency comb formation. One is by actively mode-locked lasers, where an external modulator alters the round-trip frequency, the other

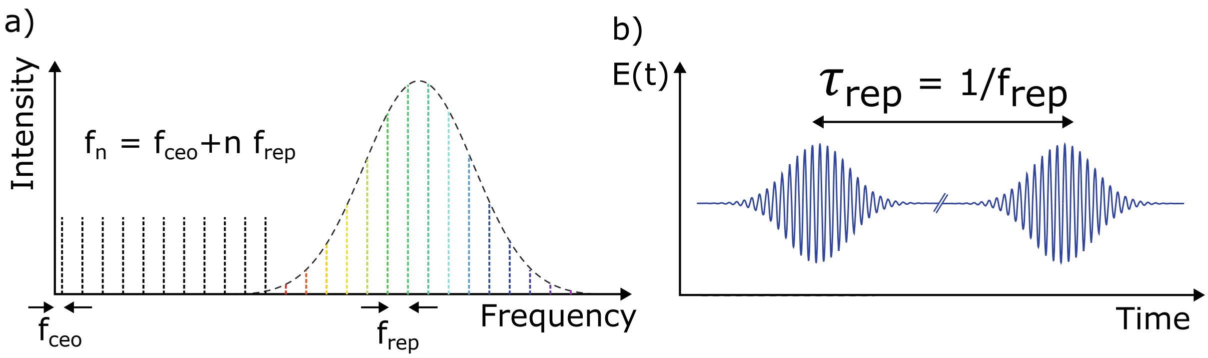

Figure 2.8: In the frequency domain (a) the modes are equally spaced with the repetition rate f_{rep} and the distance from the first (virtual) mode to the origin f_{ceo}. In the case of AM, the laser emits pulses with a time separation equal to the inverse of the repetition rate of the laser in the time domain b).

is by passively mode-locked lasers, where the modulation typically is caused by saturable absorbers or nonlinearities [63, 64].

The polarization of a nonlinear medium can be expanded as a Taylor series:

$$\mathbf{P}(t) = \varepsilon_0 \left(\chi^{(1)}\mathbf{E}(t) + \chi^{(2)}\mathbf{E}^2(t) + \chi^{(3)}\mathbf{E}^3(t) + \ldots \right), \tag{2.60}$$

where $\chi^{(3)}$ denotes the third-order susceptibility.

Experiments have shown that the active region of quantum cascade lasers exhibits a very high third-order nonlinearity $\chi^{(3)}$, which enables four-wave mixing (FWM) [60, 64]. The third-order susceptibility can be expressed as

$$\begin{aligned}\chi^{(3)}(\Delta, \delta\omega) = \frac{2\delta N_0 (q \cdot z_{ij})^4}{3\epsilon_0 \hbar^3} & \frac{(\delta\omega - \Delta - i/T_2)(-\delta\omega + 2i/T_2)(\Delta + i/T_2)^{-1}}{(\Delta - \delta\omega + i/T_2)(\delta\omega - i/T_1)} \\ & \times \frac{1}{(\delta\omega - \Delta - i/T_2)(\delta\omega + \Delta - i/T_2)},\end{aligned} \tag{2.61}$$

where δN_0 is the population inversion, z_{ij} is the dipole moment, $\Delta = \omega_1 - \omega_{12}$ is the detuning from the intersubband transition, and $\delta\omega = \omega_1 - \omega_2$ is the difference between the two incident frequencies [64].
The principle of degenerate FWM is depicted in Figure 2.9. Four waves with frequencies ω_1, ω_2, ω_3, and ω_4 interact in a way that $\omega_3 = 2\omega_1 - \omega_2 = \omega_1 - \delta\omega$ and $\omega_4 = 2\omega_2 - \omega_1 = \omega_2 + \delta\omega$, thereby creating an equally spaced frequency comb.

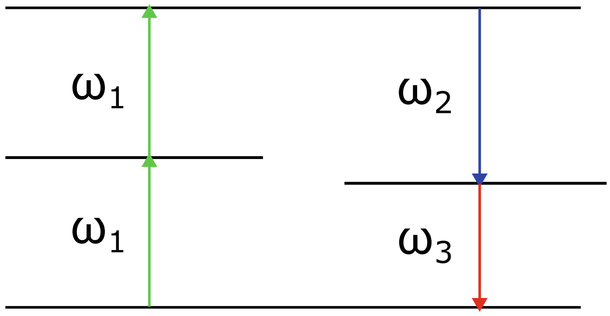

Figure 2.9: Principle of degenerate four-wave mixing (FWM)

2.4.2 Injection Locking

The frequency between two adjacent comb frequencies f_{rep} is typically in the RF range and can therefore be measured electrically directly at the voltage probes of the QCL [65]. In the same way, it is possible to inject an RF signal close to the round-trip frequency f_{rep}, thereby locking it to the RF signal [65–67].

CHAPTER 3

Methods

3.1 Design

As described in detail in section 2.3, the far-field power depends strongly on the bending radius. Therefore, by varying the radius along the perimeter, the far-field varies accordingly. For segments with different radii, Euler bends are used due to their unique properties, as described in section 2.3.1. For designing such geometries, it is very convenient to use the Python library *Nazca Design*, which is a special library for designing waveguides and photonic integrated circuits.

In principle, there are indefinite possibilities for varying the radius along the perimeter. The main challenge is the size of the laser which has to be reasonably small, and the change in radius which should be as slow as possible. Therefore, two different designs were tested: namely, egg-shaped resonators (4 Euler bends) and pan-shaped resonators (2 Euler bends).

As discussed in detail in Chapter 4, one of the main challenges is the optimization of both the bend radii and the bend angles.
Since there is no analytic solution for the start and end coordinates of Euler bends (see Equation 2.44), a numerical approach is necessary. The end coordinate of an Euler bend depends on the angle ϕ, the radius R_c, and the length of the curve s_0.
Using Equation (2.40c), we find that ϕ, R_c, and s_0 are not independent but instead follow the relation:

$$s_0 = 2R_c\phi. \tag{3.1}$$

Consequently, the Euler bend is fully defined by ϕ and R_c.

As illustrated in Figure 4.1, the waveguides consist of either two or four Euler bends positioned between two circular arc sections, forming a closed loop. Therefore, it is necessary to find an angle ϕ for all Euler bends such that a closed loop is formed.

In the case of two Euler bends, if the angles and radii of the small and large circular arcs are set, it is necessary to find appropriate bend angles ϕ for both Euler bends to satisfy Equation (4.1) and form a closed loop. This can be achieved through an iterative process.

This process becomes more complex when using four Euler bends. One approach is to use a fixed value for the reverse angle (Euler Bends 2 and 3 in Figure 4.1), as described in Section 4.2, and optimize the angles of the remaining Euler bends to satisfy Equation 4.3.

3.1.1 Size Optimization

Due to increased waveguide losses, the bend radii cannot be made arbitrarily small, which makes it essential to optimize the angles to achieve the smallest possible overall size. In the case of two Euler bends, only the angles of the small and large circular arcs can be adjusted. This can be done by an iterative algorithm that adjusts both angles until the minimum achievable size is reached.

In the case of four Euler bends, the optimization becomes more complex. Not only can the angles of the two circular arc sections be varied, but the angle of the reverse Euler bend can also be adjusted, adding further complexity to the optimization process.

3.2 Simulation

Due to the complexity of the geometries, numerical simulations of the electrical and optical properties are necessary. These were performed using a commercial finite-element solver (COMSOL Multiphysics 6.1). Figure 3.1 shows a screenshot of the simulated geometries. The waveguide is made of undoped GaAs (blue) and is surrounded by vacuum (grey). The outer half sphere consists of a perfectly matched layer (PML), which absorbs all outgoing radiation. The far-field is calculated on the inner surface of this half sphere.
The top of the waveguide as well as entire bottom plane of the half sphere are perfect electric conductors.

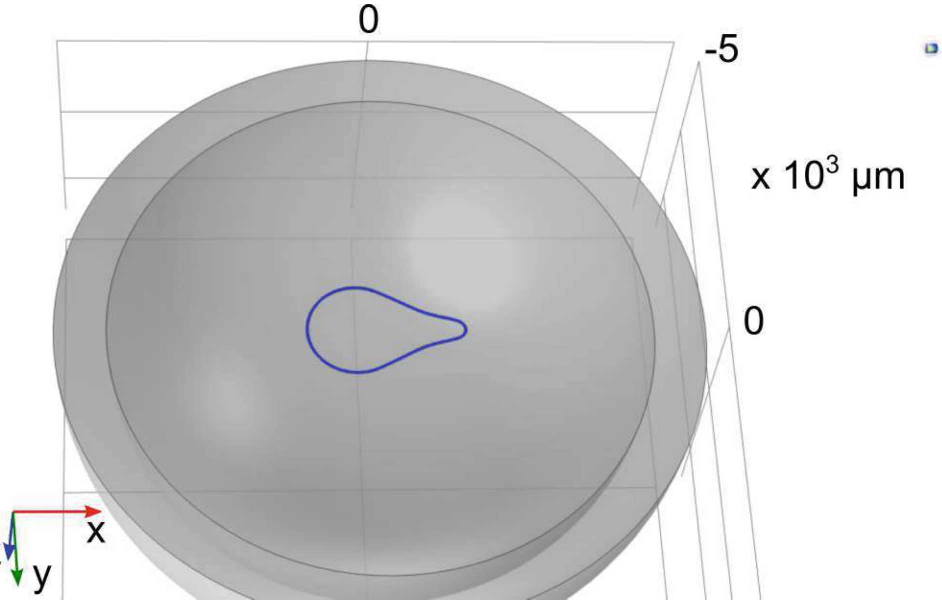

Figure 3.1: Screenshot of the geometry of a typical simulation with the waveguide (blue) in the center of the far-field domain.

3.3 Processing of the Laser

As described in section 2.2, DMWGs are most commonly used for QCLs and therefore used for all lasers presented in this thesis.

The active region (section 2.1.2) is cleaved into a 10 mm by 10 mm piece as well as an 11x11 mm n+ GaAs substrate. On both pieces, a Ti/Au (10/1000 nm) layer is deposited by sputtering (Figure 3.3a). The active region is flip-chip bonded onto the substrate by a thermo-compression wafer bonding process. This is done by using an EVG 501 and applying a constant pressure of about 4.5 MPa at 330 °C for about 30 minutes (Figure 3.3b).

The active region is removed by polishing and wet-etching (H2O2 + NH4OH). A layer with very high aluminium content ($Al_{0.55}Ga_{0.45}As$) is implemented during MBE growth and serves as an etch stop layer, which can be removed by wet-etching with concentrated HF (38 %) (Figure 3.3c).

The active region is structured with optical lithography using a positive photoresist (AZ 5214-E used as positive resist) and a laser writer (Heidelberg MLA150) (Figure 3.3d). By sputtering a thin Ti/Au (10/500 nm) layer onto the top surface of the active region and employing a lift-off process, the footprint of the structure is created (Figure 3.3e).

The top gold layer serves as a self-aligned etching mask for the anisotropic reactive ion etching process (Oxford Plasmalab System 100). This process ensures vertical sidewalls due to its anisotropic nature (Figure 3.3f).

After cleaving the sample, it is indium soldered onto a copper plate. For the electrical contacts, a small printed circuit board (PCB) is glued to the copper plate next to the

sample. The lasers and the PCB are connected with a thin (25 μm) gold wire.
Figure 3.2 shows the copper plate with five lasers already wire-bonded to the PCB.

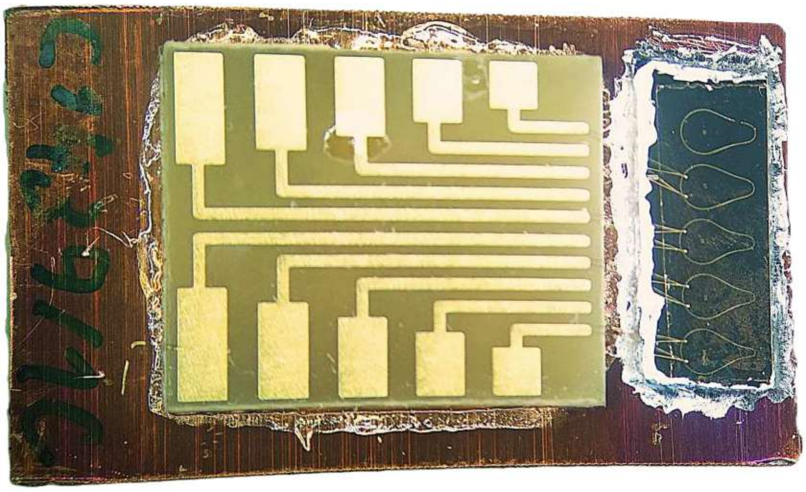

Figure 3.2: Mounted and wire bonded sample with five lasers

3.4 Measurement Setup

The principal measurement setup is shown in Figure 3.4. The sample is placed on a sample holder (Figure 3.8), which is mounted onto the cold finger. Due to the low operating temperature of QCLs, the laser is cooled down to about 4.7 K with liquid helium. To prevent condensation, the cryostat must be evacuated with a turbo pump.
In front of the laser is a THz-transparent window made of TPX. The light is guided through the window into a Fourier transform infrared spectrometer (FTIR) (Bruker Vertex 80) by a parabolic mirror, which collects the emitted light within an angle of 28 degrees. Inside the FTIR is a pyroelectric crystal (DTGS), which is used as the detector.

For the principal characterization of a laser, a light-current-voltage (LIV) measurement can be used. The LIV can be measured by sweeping the bias voltage and recording the voltage and current with an oscilloscope (Tektronix DPO 3032), while the laser intensity is measured with the DTGS detector and a lock-in amplifier (Stanford Research Systems SR830).
The laser is driven by a pulse generator (HP 8114A or AVTECH AVR-3HF-B) with pulse lengths between 500 ns and 4 μs and a repetition rate between 10 kHz and 100 kHz. Since the lock-in amplifier cannot measure at such high frequencies, the pulse generator is gated with the trigger signal from a function generator (Agilent 33220A) with a frequency between 10 Hz and 17 Hz.

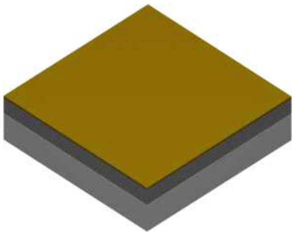

(a) Deposition of Ti/Au (10/1000 nm) on active region

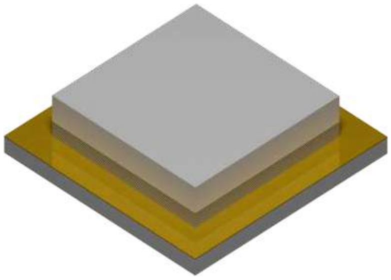

(b) Episide down flip chip bonding

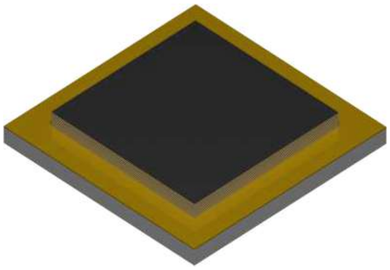

(c) Removal of the substrate by polishing and wet-etching

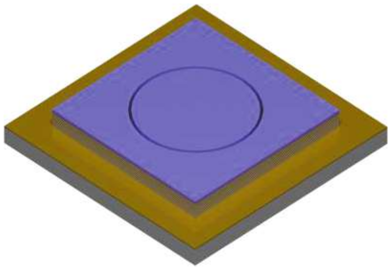

(d) Structuring the geometry of the laser by optical lithography

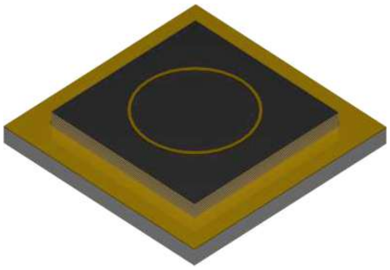

(e) Deposition of Ti/Au (10/500 nm) on active region by using a lift-off process

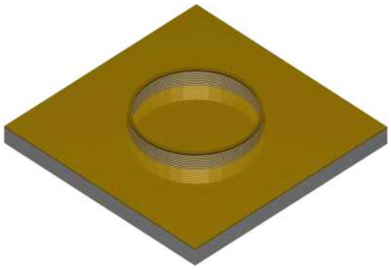

(f) Reactive ion etching: gold acts as etching mask

Figure 3.3: Illustration of the processing of a double-metal ring laser.

Spectral measurements are performed with the FTIR, which achieves a spectral resolution of 2.5 GHz.
To measure the spectrum in cw mode, the pulse generator is replaced with a DC source-measurement unit (SMU, Keithley 2602A).

For measuring electrical beat note signals created by the comb operation, as well as for RF injection (see Section 2.4.2), an additional semi-rigid RF line is implemented (Figure 3.4), equipped with a DC block to allow only the desired RF signal to pass.
By using an RF circulator, it is also possible to inject an RF signal over the same line. A circulator has three ports, where the signal can only pass from Port 1 to 2, 2 to 3, and 3 to 1, hence the name circulator.

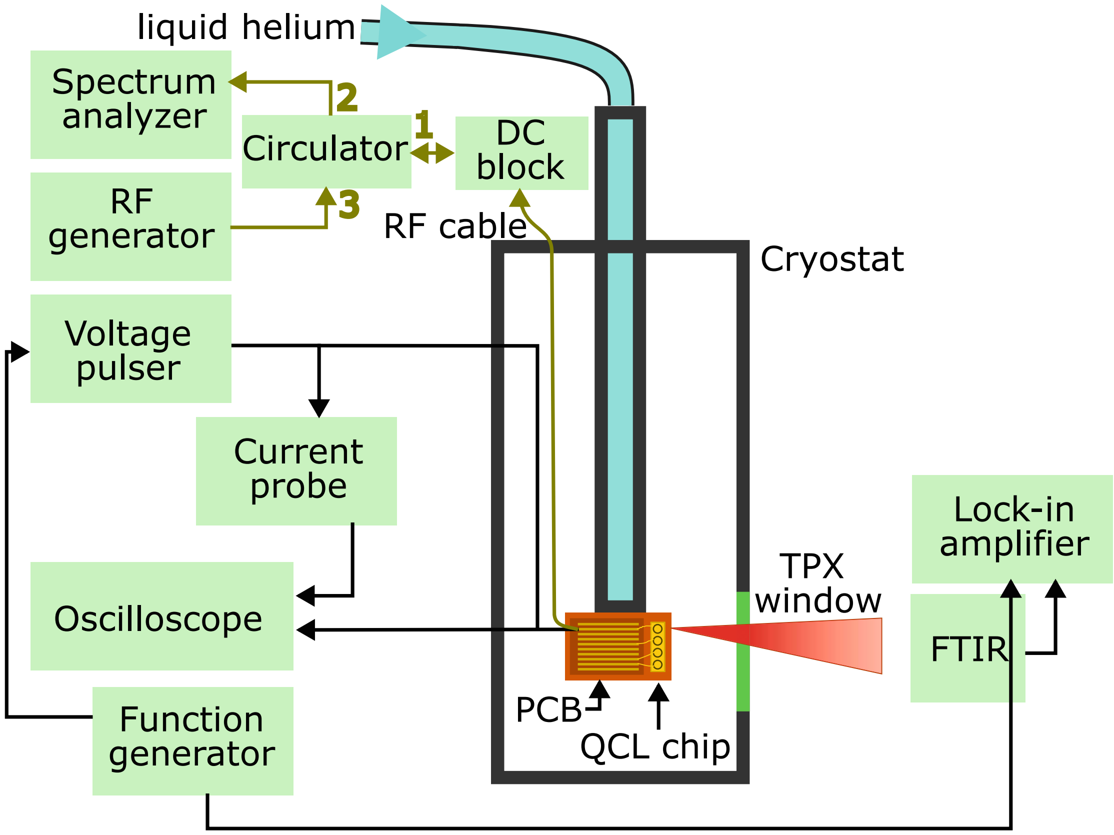

Figure 3.4: Illustration of the measurement setup including the RF cable for RF injection and measurement.

3.4.1 Far-Field

To measure the far-field of a device, the same setup described in 3.4 can be used, with the addition that the pyroelectric detector is mounted on a stage that can move in the vertical and horizontal directions, as illustrated in Figure 3.5. For this purpose, a stage with two stepper motors is used for measuring the far-field intensity over an area of several square centimeters typically with a resolution ranging from 15×15 to 35×35 data points. The time constant of the lock-in amplifier is typically set to 0.3 s. Therefore, a waiting time between two adjacent measuring points of 0.9 seconds is necessary to obtain accurate results. This limits the number of data points significantly due to time constraints.

Although the scanning is performed in Cartesian coordinates, it is often more convenient to represent the data in polar coordinates. The coordinate system, defined in terms of r, θ, and φ, is illustrated in Figure 3.5 and 3.6, with the origin defined as the position of the laser.

To achieve accurate data, it is essential to precisely determine the position of the detector relative to the laser. Both the cryostat and the stage are mounted on a laser table, with the zero position ($\theta = 0$, $\varphi = 0$) of the coordinate system defined as the intersection of the plane parallel to the laser table and the plane parallel to the copper plate, both intersecting the laser. The distance z is defined as the distance between the detector and the laser along the line where $\theta = 0$ and $\varphi = 0$. Therefore, the radius r is a function of the x and y position of the detector ($r = r(x, y)$).

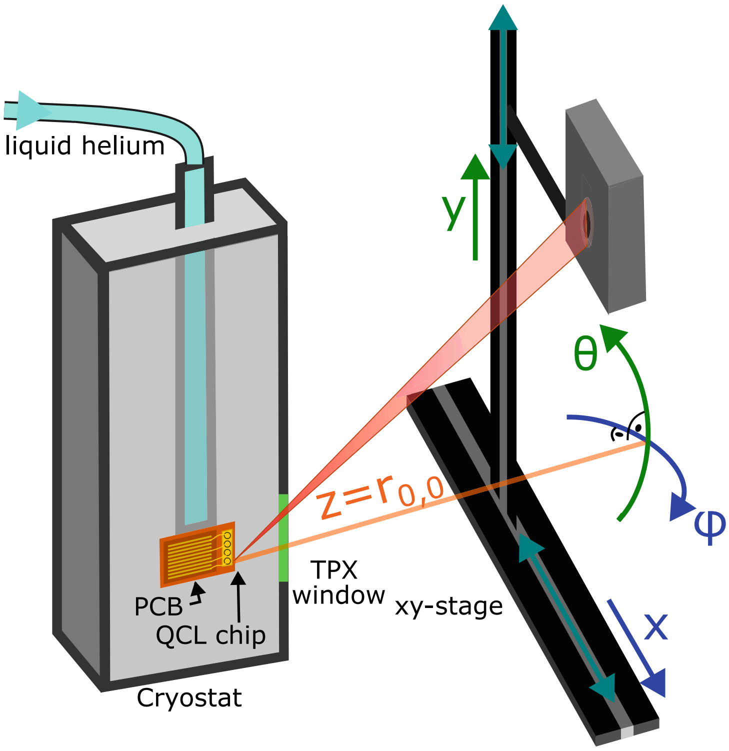

Figure 3.5: Setup for measuring the far-field including the coordinate system in polar coordinates. A wire grid polarizer can be placed between the laser and the sensor to measure the polarization of the far-field (not shown).

For aligning the laser with the detector, an alignment laser is used, as illustrated in Figure 3.7. By using two optical posts of the same length, one on each side of the cryostat, it is possible to align the laser to the plane parallel to the optical table and also to the plane parallel to the copper plate.
Using the laser beam, it is straightforward to center the QCL precisely in the center of the beam by using the xyz-stage to which the cryostat is mounted. Similarly, the detector is positioned at the center of the beam using the motorized xy-stage.
Therefore, the position of the laser in terms of r, φ, θ can be recalculated from the x, y, z coordinates for any arbitrary position.

The coordinate transformation from Cartesian coordinates to spherical coordinates is

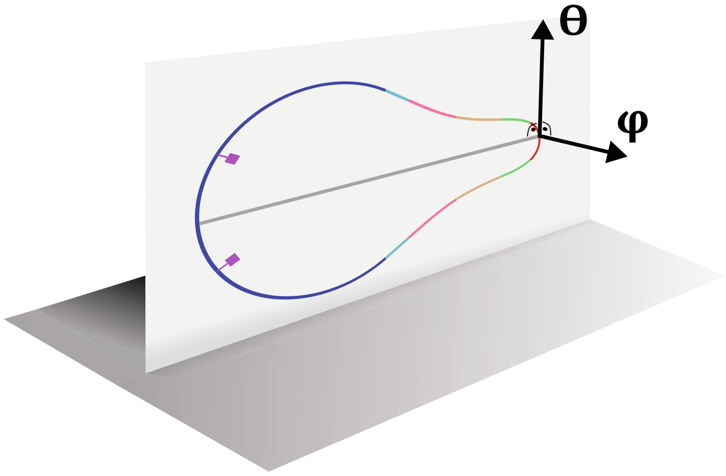

Figure 3.6: Coordinate system in terms of θ and φ used for all far-field measurements, with the device placed vertically inside the cryostat.

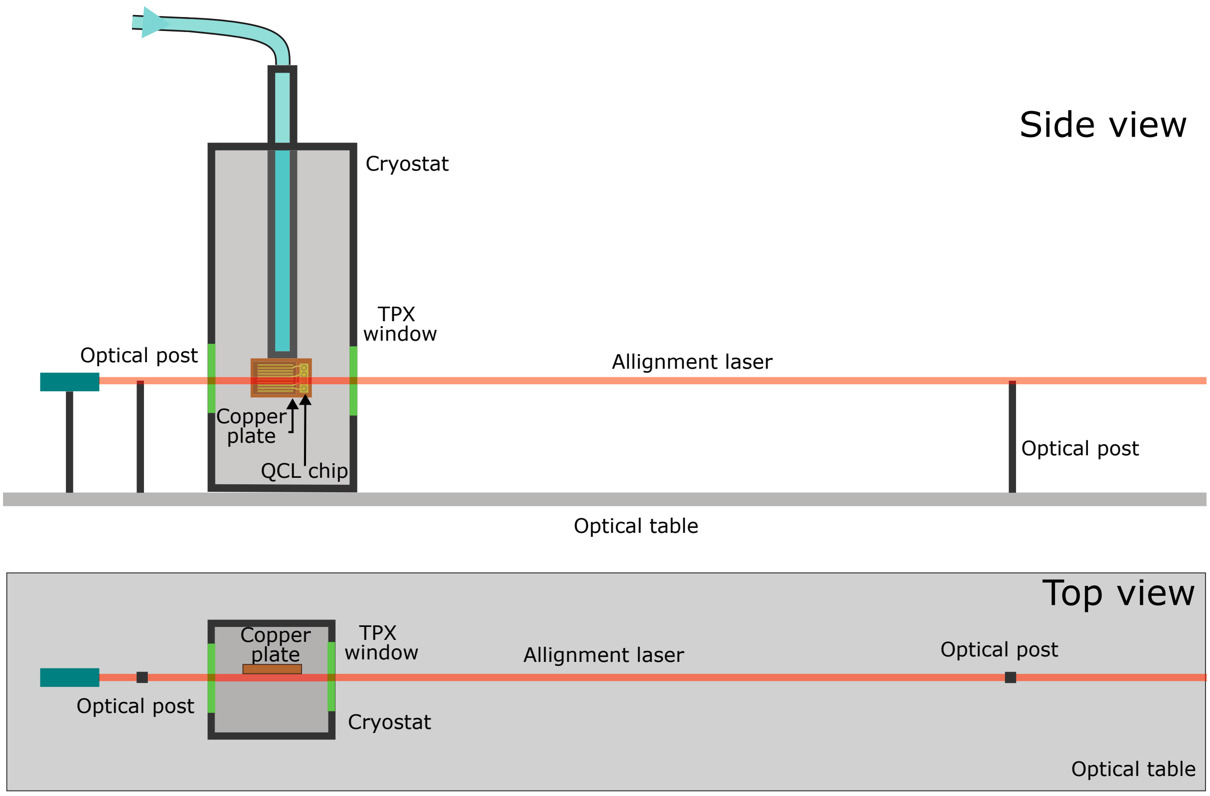

Figure 3.7: Illustration of the alignment setup for determining an accurate zero position

defined as:

$$r = \sqrt{x^2 + y^2 + z^2} \tag{3.2a}$$

$$\theta = \arccos\left(\frac{z}{r}\right) \tag{3.2b}$$

$$\varphi = \text{atan2}(y, x). \tag{3.2c}$$

3.4.2 Submount

Due to the complex far-field and the limited size of the window in the cryostat, a special submount for the coldfinger is necessary to ensure that the light can reach the detector. Therefore, it is necessary that the laser can be tilted in the Θ and φ directions. As a result, a custom submount was built, as shown in Figure 3.8. By loosening a screw at the back (not visible), the top plate can be rotated 180 degrees in the Θ direction. The coldfinger itself can also be rotated in the φ direction, therefore allowing the laser to be rotated in any arbitrary direction.

To ensure good heat conduction between the laser and the coldfinger, a thermal paste was applied between all copper interfaces.

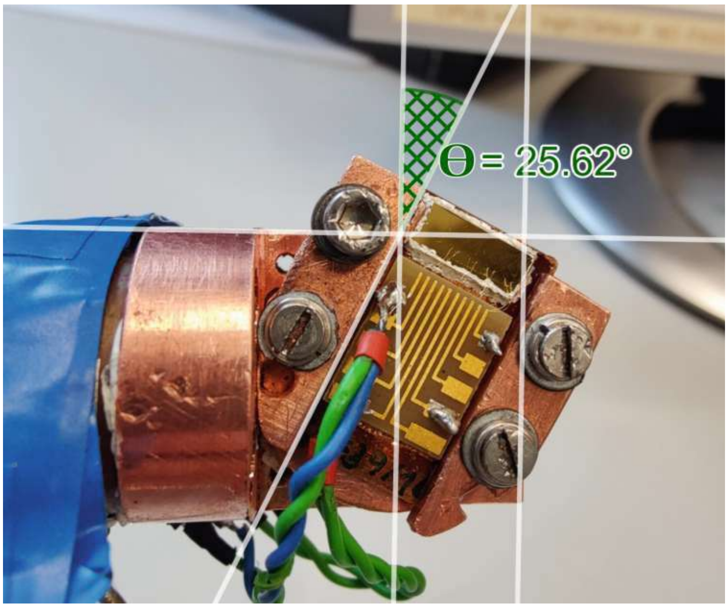

Figure 3.8: Custom-built submount that enables tilting the laser in the Θ direction. The already mounted and connected QCL is rotated to $\Theta = 25$ degree.

Data Visualization

The plotting and coordinate transformation are done using Python. Due to the limited number of data points, interpolation can significantly improve the quality of the data. For this purpose, an radial basis function (RBF) interpolation with a multiquadratic kernel is used.

The interpolation not only enhances the visual appearance but also extends the possibilities for analysis. For better comparison between different measurements, the full width at half maximum (FWHM) was calculated based on the interpolated data. The FWHM is defined as the signal width at half the maximum intensity. Since the FWHM typically forms a loop, it is appropriate to define two discrete values: one for the shortest distance and one for the longest distance between the maximum intensity and the half maximum.

CHAPTER 4

Results

4.1 Egg-shaped Resonators

For the egg-shaped resonator, two arc sections are connected by two Euler bends (labeled as 1 and 2), as shown in Figure 4.1 a). This design allows the overall footprint to remain relatively small.
To maintain the egg shape, the total bend angle must equal 360 degrees. Consequently, the total bend angle of the small and large arc sections must be significantly smaller than 360 degrees to fulfill equation 4.1, with the bend angles of the small and large circular arc sections a_s and a_l, and the bend angles of the Euler bends e_1, e_2.

$$360 = a_s + 2(e_1 + e_2) + a_l \tag{4.1}$$

According to Equation (3.1), for a constant end radius R_c, a smaller bend angle results in a shorter length s_0 but leads to an increased change in curvature. By using Formulas 2.38 and 2.40a, we can derive the relation:

$$\frac{d^2\phi}{ds^2} = \frac{1}{R_c\, s_0} \tag{4.2}$$

for the change in curvature.
To keep this change low, it is therefore essential to make the Euler bend as long as possible. However, to maintain a compact design, it is important to limit the length of the Euler bends, especially for Euler bend 2, due to its larger end radius and consequently increased length. Consequently the large circular arc section should have a bend angle of at least 180 degrees, and the bend angle of the small circular arc should ideally remain below

90 degrees.
Another important consideration is the outcoupling power, which depends strongly on both the radius and the waveguide length. Therefore, the length of the small circular arc section should be maximized to optimize outcoupling.
Overall, the egg shape is suitable for small differences in radius but has the drawback of a short arc section on the outcoupling side.

4.2 Pan-shaped Resonators

To overcome the limitations of the egg-shaped resonators, one can use four Euler bends instead of two for connecting the circular arc sections. As shown in Figure 4.1 b), the curvature of the Euler bends labeled 1 and 2 has the same sign as the two circular arc sections, whereas the sign of the curvature of sections 2 and 3 is inverted. Therefore, equation 4.3, with the bend angles of the small and large circular arc sections a_s and a_l, and the bend angles of the Euler bends e_1, e_2, e_3, and e_4, must be satisfied:

$$360 = a_s + 2(e_1 - e_2 - e_3 + e_4) + a_l \tag{4.3}$$

It turned out that for a small overall size and shallow changes in radius, the bend angles of sections 1 and 4, as well as sections 2 and 3, should be equal. Consequently, we can rewrite equation 4.3 as:

$$360 = a_s + a_l + 4(e_1 + e_2) \tag{4.4}$$

Thus, only three variables need to be defined. In practice, it makes sense to define a_s, a_l, and the reverse angle $e_2 = e_3$. The angle $e_1 = e_4$ results from the closed loop condition as described in Section 3.1.

4.3 Simulations

Multiple different designs with varying sizes, angles, and radii were simulated and analyzed. Therefore, only a small selection can be presented and discussed.
According to Figure 2.4, the radius of the large circular arc section should be at least 750 μm to reduce waveguide losses. The radius of the small arc section has to be significantly smaller, in the range of 100 to 350 μm, which should result in a difference in radiated power of up to 100 dB per unit length.
For the four Euler bend case, the reverse bend should also have a radius as large as possible, but due to size constraints, it had to be limited to 400 μm. Although this is significantly smaller than the 750 μm radius of the large circular arc section, the length of

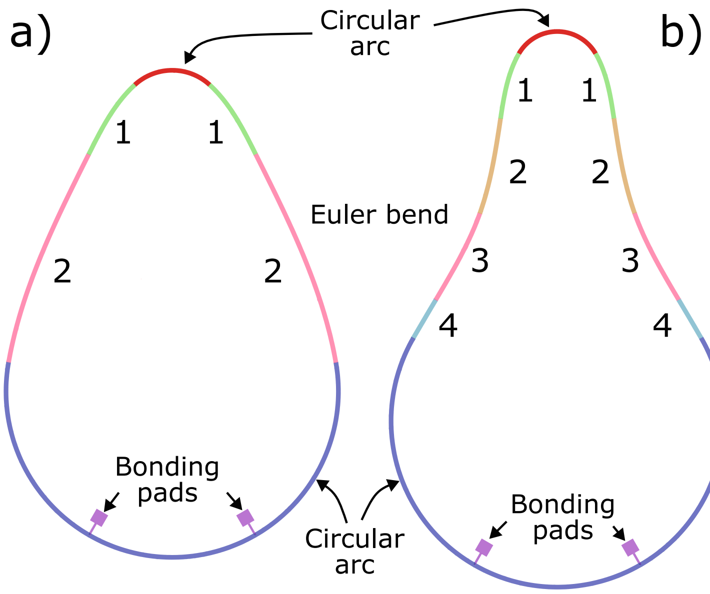

Figure 4.1: Comparison between egg-shaped resonators (a) and pan-shaped resonators (b).

the high curvature section is very short, which should limit waveguide losses.

According to formula 4.2, the change in curvature over the length of Euler bends is equal to $1/(R_c s_0)$. As a result, the Euler bends should be as long as possible to prevent unwanted effects like mode bouncing and high waveguide losses. Therefore, the size of the structure can only be reduced to a certain degree.
Figure 4.2 shows a simulation of a device with four Euler bends. The energy density of the mode shows very distinct mode bouncing, which is likely due to too fast changes in curvature.

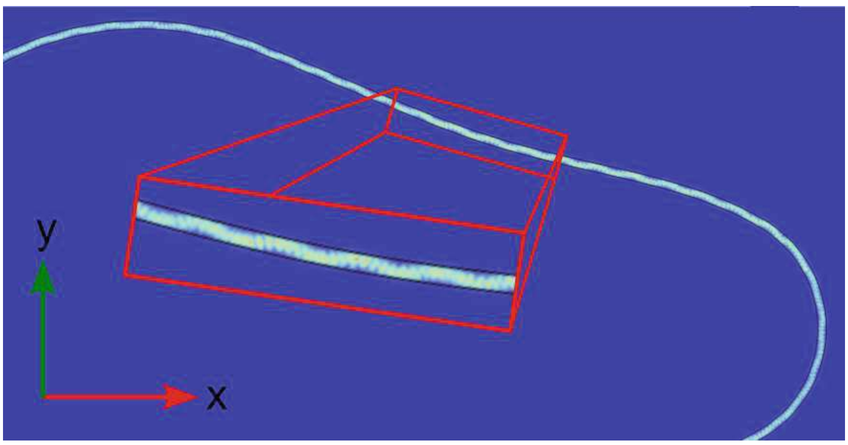

Figure 4.2: Energy density of the mode in a device with four Euler bends showing very strong mode bouncing.

Tables 4.1 and 4.2 show the design parameters of the optimized devices. The radius of the large circular section is 750 μm for all devices the minimum radius of the reverse bend is 400 μm.

Design No.	**22**	**23**	**24**	**25**	**26**
width in μm	21	21	21	21	21
r_{small} in μm	300	250	200	150	350
small arc angle in degree	95	85	75	65	95
large arc angle in degree	200	200	200	200	185

Table 4.1: Parameters for waveguide designs with 2 Euler bends

Design No.	**17**	**18**	**19**	**20**	**21**
width	21	21	21	21	21
r_{small} in μm	250	200	150	100	300
small arc angle in degree	120	120	120	116	140
large arc angle in degree	210	240	230	230	220
reverse euler angle in degree	11	11	10	13	6

Table 4.2: Parameters for waveguide designs with 4 Euler bends

The used active region has a height of 13 μm and emits between 2.3 and 2.4 GHz. Therefore, all simulations were carried out with these parameters.
Figure 4.3 shows the simulated far-field of device 17, while Figure 4.4 shows the electric field in the z-direction for the same device. Due to the much shallower changes in curvature, the mode bouncing is significantly reduced compared to Figure 4.2.

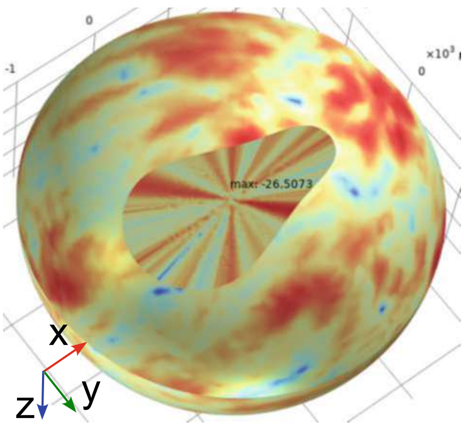

Figure 4.3: Far-field simulation of device 17

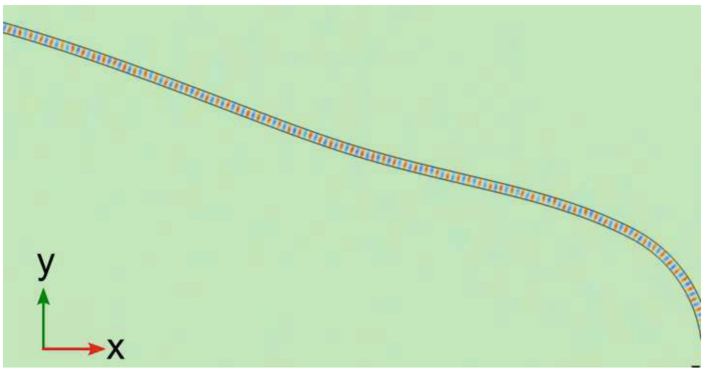

Figure 4.4: Simulation of the electric field in z direction of device 17

As described in Section 2.3.2, the group velocity dispersion is another important aspect to consider and was therefore simulated. Figure 4.5 shows the exemplary simulation results for an outer radius of 1200 μm. The GVD tends to approach zero for devices with smaller widths. However, as shown in Figure 2.5, the radiated power increases drastically for widths below 30 μm. Therefore, a waveguide width of 21 μm was chosen, which should limit the radiative losses to about 10 dB above the minimum value.

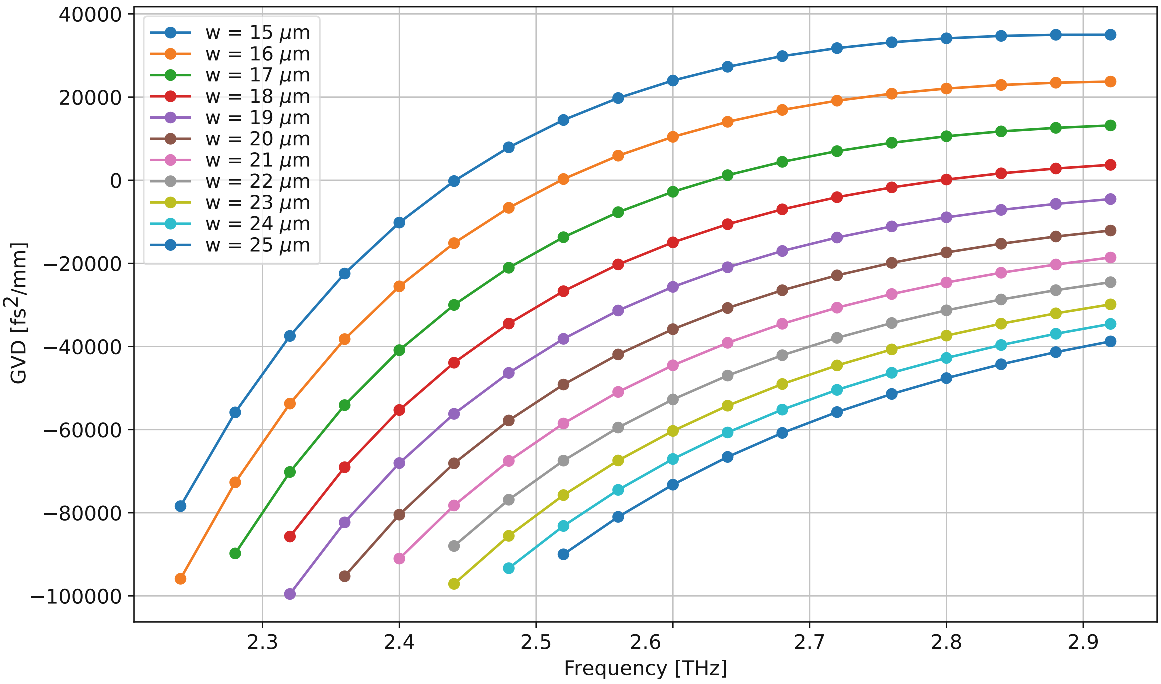

Figure 4.5: Simulated GVD for multiple waveguide widths with an outer radius of 1200 μm, considering material dispersion as defined in Equation 2.45.

Based on the simulation results, 10 different devices were selected and processed (Tables 4.1 and 4.2). The mask used for the optical lithography is shown in Figure 4.6. The numbers at the center of the devices correspond to the device numbers.

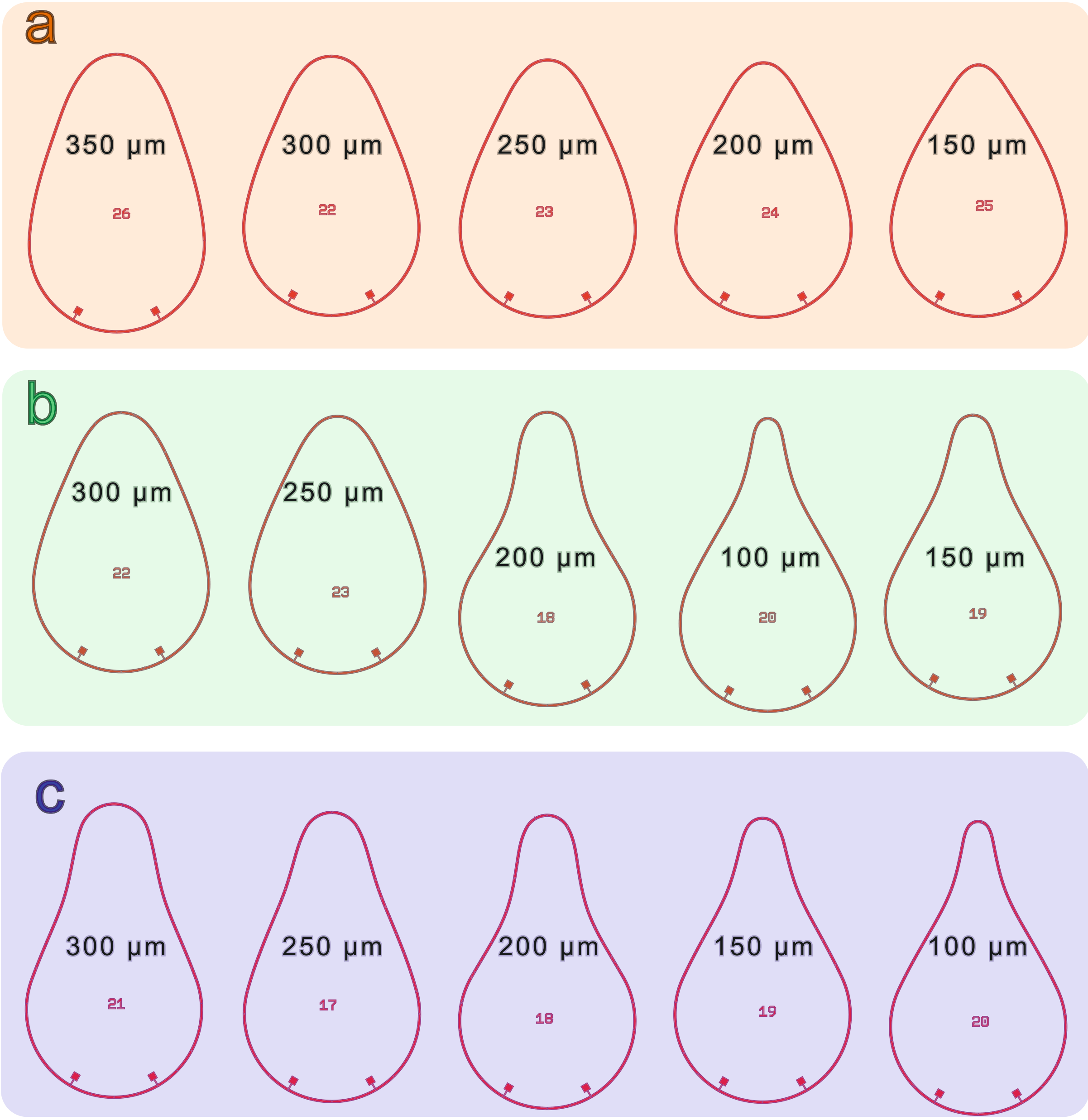

Figure 4.6: Mask used for the optical lithography consisting of 10 different devices, numbered according to Table 4.1 and Table 4.2. The processed sample is cleaved horizontally between the devices. The rows are therefore denoted as a, b, and c, which are individually mounted onto a PCB. The value inside each device denotes the minimum radius in μm.

4.4 Measurements

The devices are characterized by several types of measurements, including LIV, spectral, and far-field measurements. Due to the large number of measurements, only a subset can be shown in detail.

4.4.1 LIV and spectral measurements

Table 4.3: Threshold current density and maximum current density at a heat sink temperature of 5 K and a duty cycle of 5 % for different devices. Sample a, b, and c denoted according to Figure 4.6.

Device	Sample	Threshold Current (kA/cm²)	Max Current (kA/cm²)
Pan 17	c	0.24	0.30
Pan 18	b	0.22	0.32
	c	0.24	0.35
Pan 19	b	0.26	0.37
	c	0.25	0.36
Pan 20	c	0.25	0.36
Egg 22	a	0.30	0.42
Egg 23	a	0.27	0.38
	b	0.27	0.36
Egg 26	a	0.28	0.39

Pan 18

Figure 4.7 shows the LIV of device. The lasing threshold is around 0.25 kA/cm^2. The intensity increases fairly linear until it reaches the maximum intensity which is at approximately 3.6 kA/cm^2. By further increasing the bias voltage, the device enters the negative differential resistance (NDR) region, where the operation becomes unstable. The output power and the current are dropping in this region.
As shown in Figure 4.8, the device exhibits either three modes or multi-mode operation, depending on the bias voltage. The three modes occur around 2.13 THz and 2.45 THz, whereas the multi-mode operation ranges from 2.3-2.5 THz.
Figure 4.9 shows the interpolated spectrum presented in Figure 4.8. The average frequency spacing between two modes is approximately 12.5 GHz.
Since the device can operate in multi-mode, it should, in principle, be capable of generating phase locking, which can be analyzed by measuring the electrical beat note, as shown in Figure 4.10 for device 18. The beat note frequency is equal to the mode spacing, as described by formula 1.1. The measured beat note has a frequency of 12.49 GHz, which aligns well with the measured mode spacing of about 12.5 GHz.

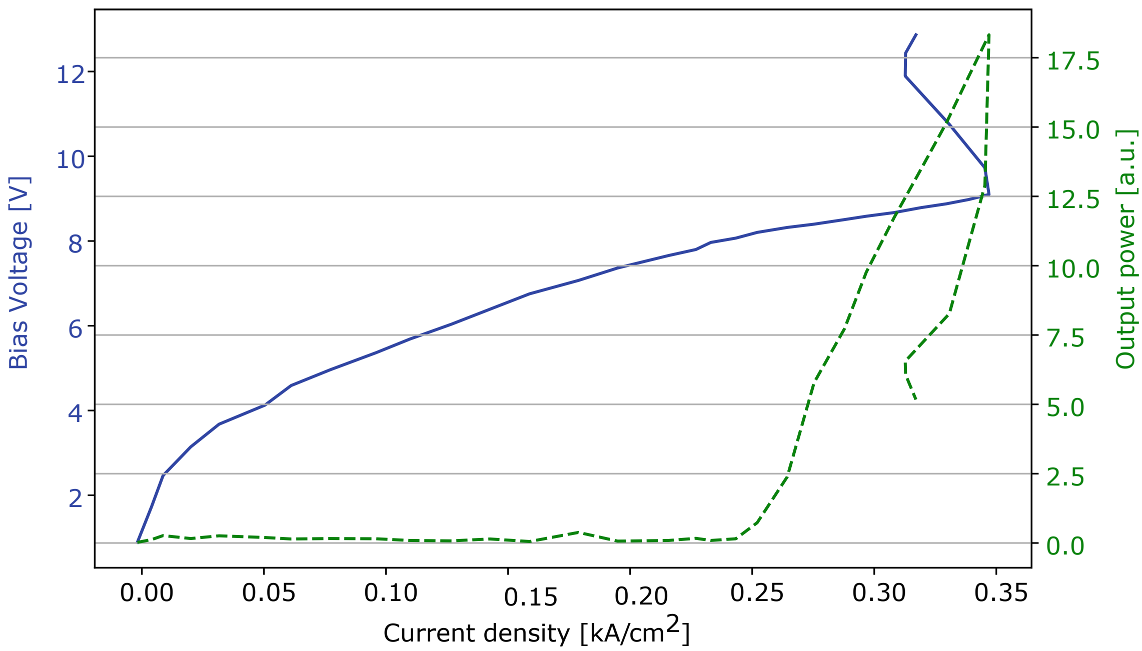

Figure 4.7: LIV of device 18 measured at 5 K and a duty cycle of 5 %. The dashed line represents the light measured with the lock-in amplifier, while the solid line shows the voltage measured on the PCB.

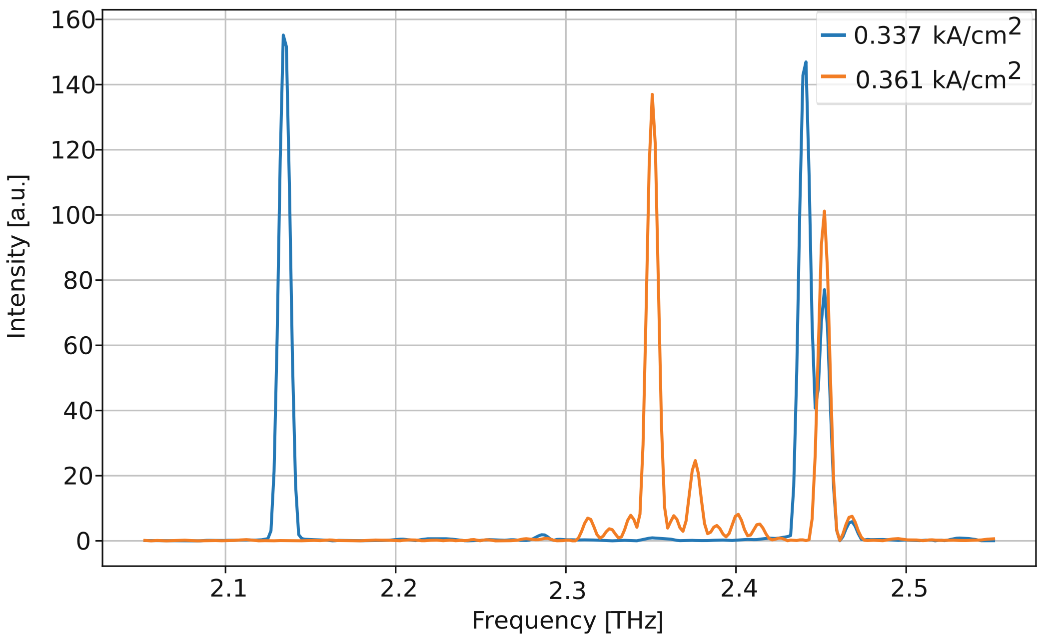

Figure 4.8: Spectrum of device 18 measured at 10 K in cw operation, showing three modes and multi-mode operation. For the multi-mode operation, a beat note was present (Figure 4.10).

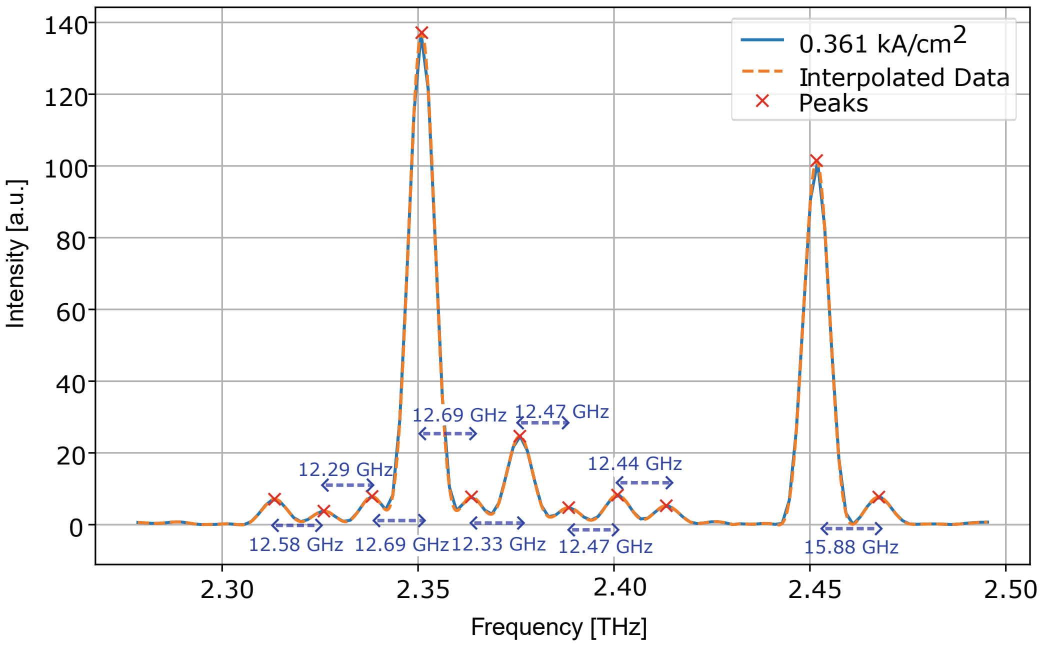

Figure 4.9: Mode spacing of device 18 in the presence of a beat note, measured at 10 K in cw operation.

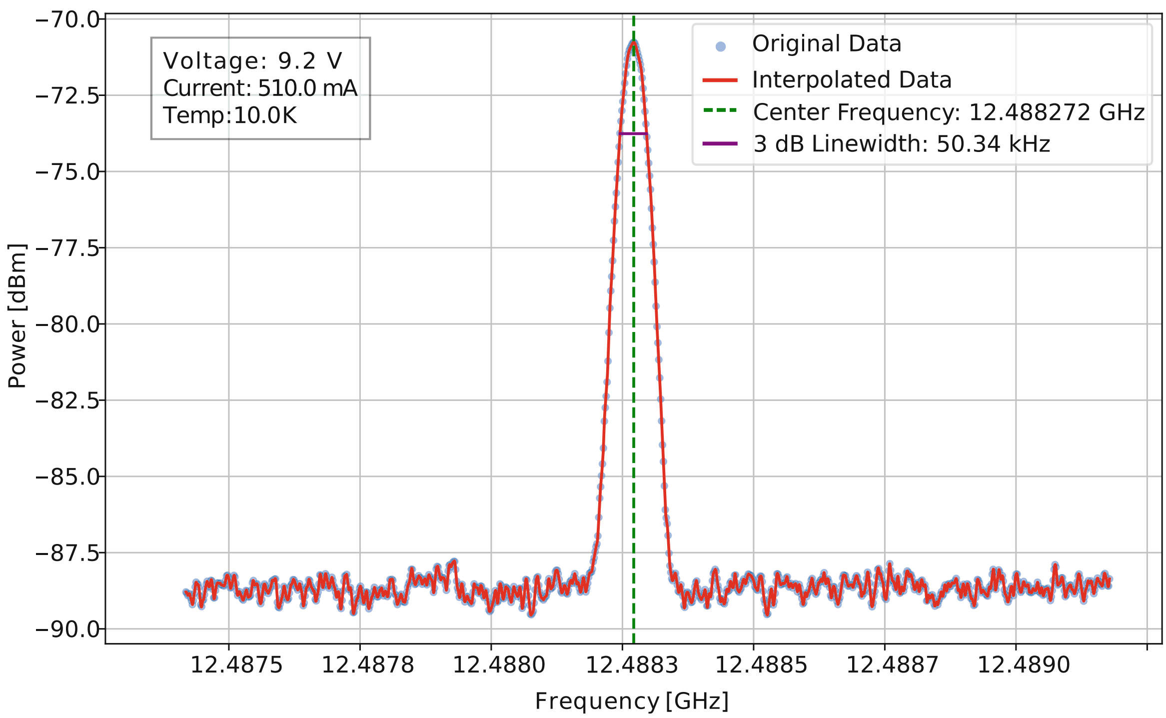

Figure 4.10: Electrical beat note of device 18 measured in cw operation. The bandwidth of the beat note is resolution limited to 51 kHz.

Egg 22

Figure 4.11 shows the LIV of device 22. The threshold current density as well as the maximum current density differ between devices 18 and 22. In general, the threshold current density of the pan designs is smaller than that of the egg designs, as Table 4.3 shows. This suggests a higher mode confinement for the pan-shaped designs. Despite this, the LIV characteristics of both devices are systematically identical.

The spectrum (Figure 4.12) does not show any signal at 2.13 THz as device 18 does (not visible in Figiure 4.12), even though the modes at 2.33 THz and 2.45 THz are clearly visible. Instead of pure multi-mode behavior, device 22 exhibits a nearly perfect single-mode operation at 2.33 THz and a multi-mode behavior between 2.35 and 2.5 THz.

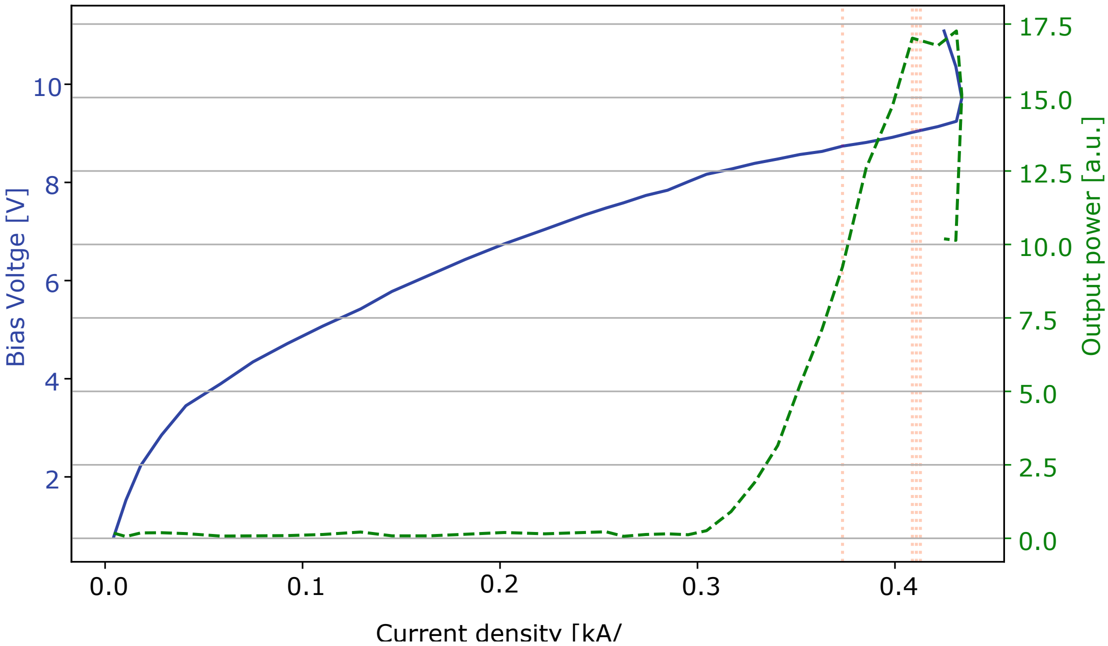

Figure 4.11: LIV of device 22 measured at 5 K and a duty cycle of 5%. The dashed line represents the light measured with the lock-in amplifier, while the solid line shows the voltage measured on the PCB. The red lines represent the measurement points in Figure 4.12.

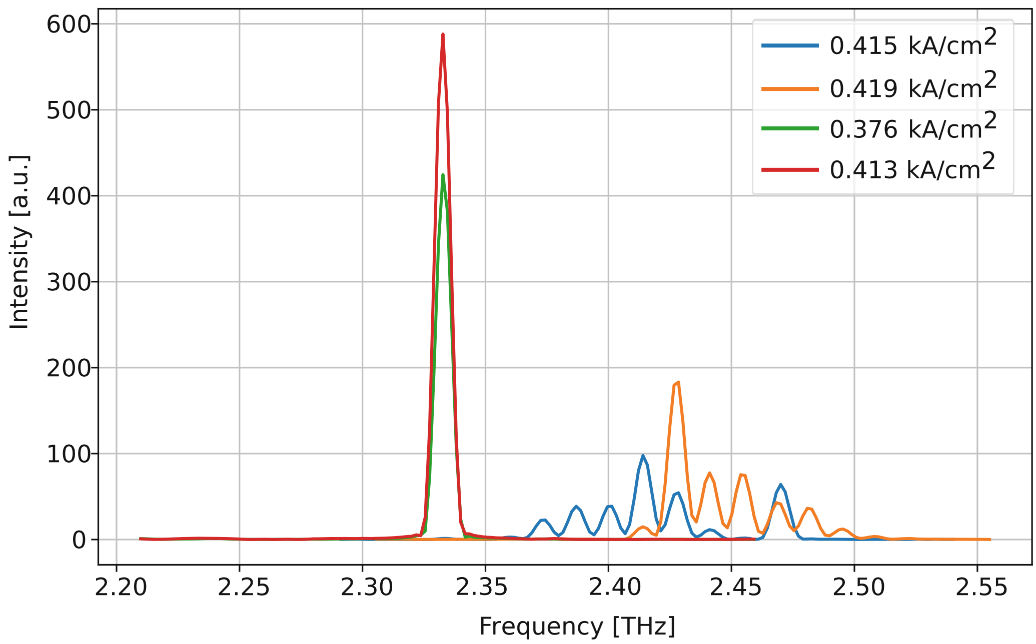

Figure 4.12: Spectrum of device 22 operating in single-mode and multi-mode. Measured at 10 K in cw operation.

4.4.2 RF Injection

As described in Section 2.4.2, it is possible to lock the comb to an injected RF signal. The injected RF signal has a frequency of 6.44 GHz, which corresponds to the first sub-harmonic of the beat note frequency. Figure 4.13 shows the spectrum of device 19, and Figure 4.14 shows the corresponding measured beat note signals with and without RF injection. By changing the RF frequency, it is possible to pull the beat note to higher and lower frequencies by up to about 2 MHz, even though the injection frequency is only half the beat note frequency. This indicates a locking of the comb to the RF signal.

Typically, the bandwidth of a beat note is expected to be on the order of a few Hz. However, in this case, the bandwidth is resolution-limited.

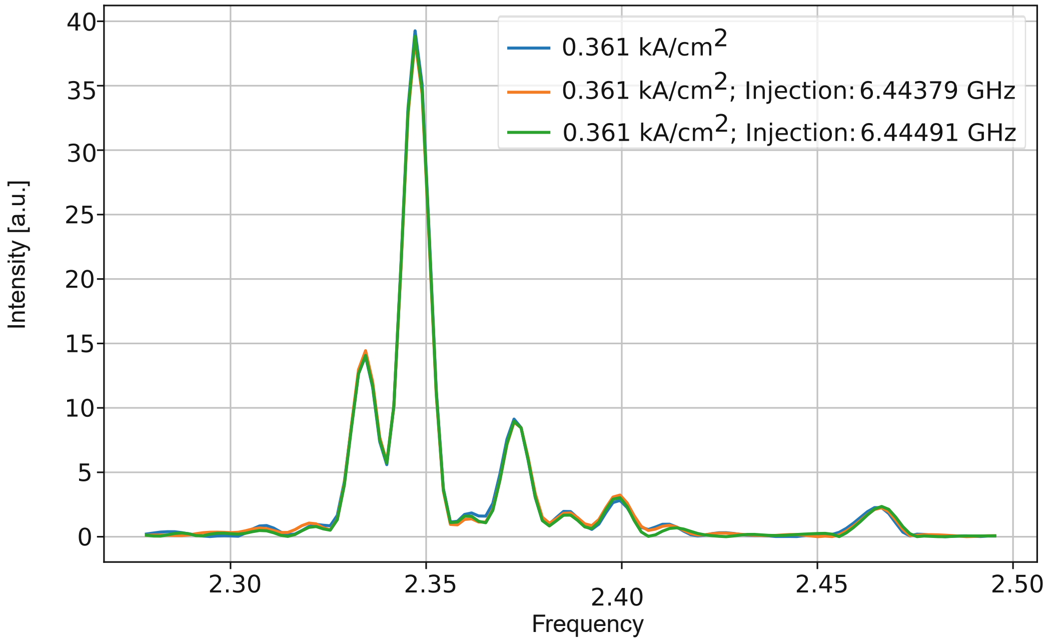

Figure 4.13: Spectrum of device 19 operating in multi-mode, measured at 10 K in cw operation. The three spectra correspond to the three beat note measurements shown in Figure.

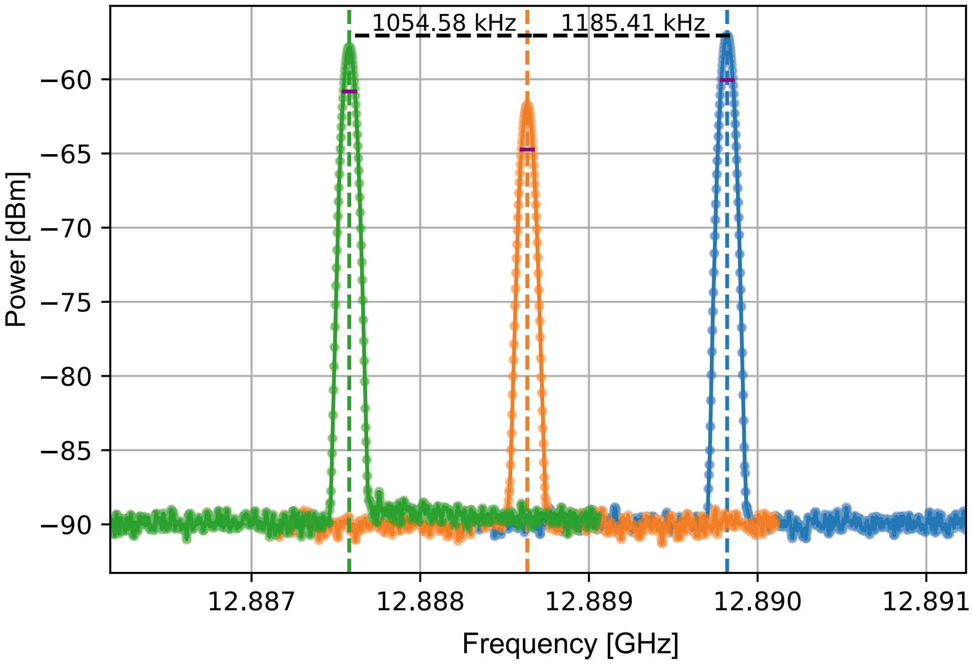

Figure 4.14: Beat note of device 19 measured in cw operation, corresponding to Figure 4.13. The dots represent the measurement points, while the solid line is an interpolation. The orange beat note in the middle represents the free-running comb with no injection and a center frequency of 12.888635 GHz. The green and blue beat notes on the left and right are measured with RF injection. For the green beat note, an injection frequency of 6.44379 GHz is used, and for the blue one, 6.44491 GHz. The bandwidth of the beat note signals is resolution-limited to 68 kHz. A maximum pulling of about 2 kHz can be achieved.

4.4.3 Far-Field Measurements

The far-field was measured for all devices in terms of the coordinates z, φ, and Θ, as defined in Figures 3.5 and 3.6. All measurements were performed with a duty cycle of 40%.

4.4.4 Reflections

One of the major challenges are reflections coming from the inside of the cryostat, which is entirely made of aluminum and thus highly reflective to THz radiation. This becomes especially problematic for ring-shaped resonators, which inherently couple light out in all directions along their perimeter.
Another difficulty is that the cylindrical window flange can act as a parabolic mirror, enhancing the intensity in some spots and altering the polarization of the light, as illustrated in Figure 4.15.

One solution to mitigate these issues is to implement a THz-absorbing foil, which absorbs about 50% of the light, thereby reducing the intensity of the reflections to approximately 25% as the light has to pass through the foil twice.
Although this significantly reduces the amount of reflections, it does not entirely solve the issue. Another approach is to place an aperture close to the cryostat, between the laser and the sensor, thereby cutting off most of the reflections.
As described in Section 2.1.3, the polarization of a QCL must be parallel to the growth direction. However, as shown in Figure 4.15, the polarization of the reflections is, with high probability, rotated to some degree. Therefore, placing a polarizer in the beam path can help distinguish between reflections and the direct signal.

By using all three of the described methods, the impact of reflections can be reduced to a very high degree.

4.4.5 Measurements

As described in Section 3.4.2 the submount can be rotated in the Θ direction. The far-field was measured with the submount rotated to $\Theta = 0°$, $\Theta = 17.5°$ and $\Theta = 35°$ degrees at distances of 9.5 cm and 22 cm.

Pan 17

Figure 4.17 shows the far-field measurement of device 17 for different aperture openings. Without the aperture, multiple reflections and interference patterns are visible. By decreasing the size of the aperture, the signal separates from the reflections due to the

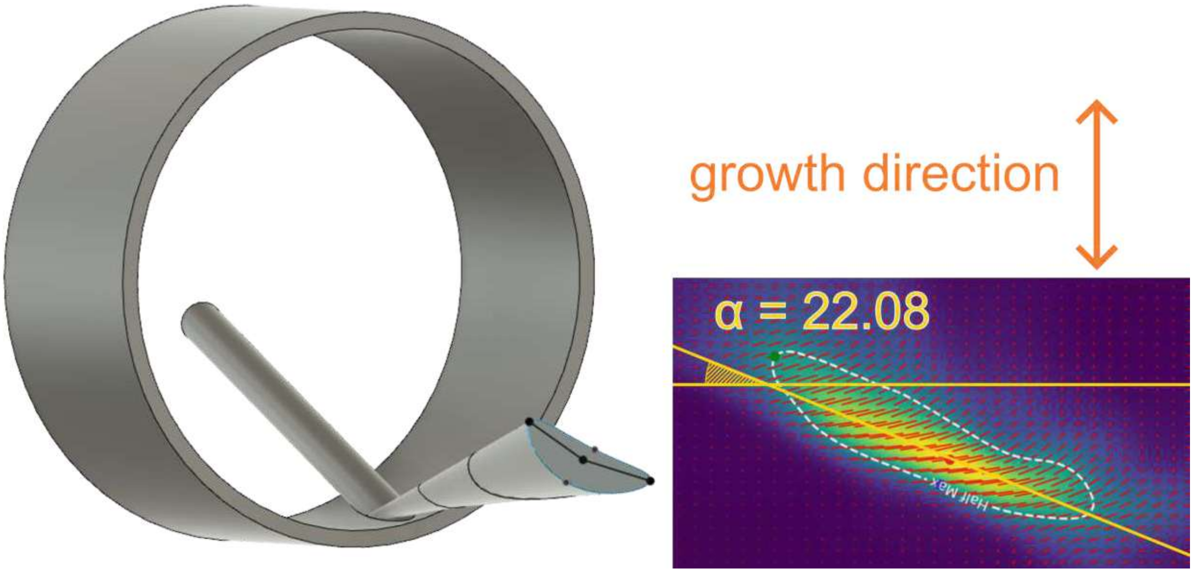

Figure 4.15: Simulation of the change in a circular beam after reflecting off the cylindrical window flange of the cryostat compared to a measured reflection. As shown, not only does the shape change, but the polarization is also altered, as indicated by the red lines in the far-field pattern. Note that the device was mounted horizontally and not vertically as for the other measurements, consequently the polarization is perpendicular to the growth direction.

Figure 4.16: Mounted sample inside the cryostat. The cylindrical window flange can be covered with THz-absorbing foil (not shown) to mitigate reflections.

different origins of the radiation.
When using an aperture of 1 cm, the closest distance from the maximum to the nearest half-maximum is 1.816 degrees, which suggests a fairly collimated beam.
Figure 4.18 shows the measured polarization. The main beam shows a nearly perfect horizontal polarization which is parallel to the growth direction.

At a distance of 22 cm, the far-field shows a distance between the maximum and the

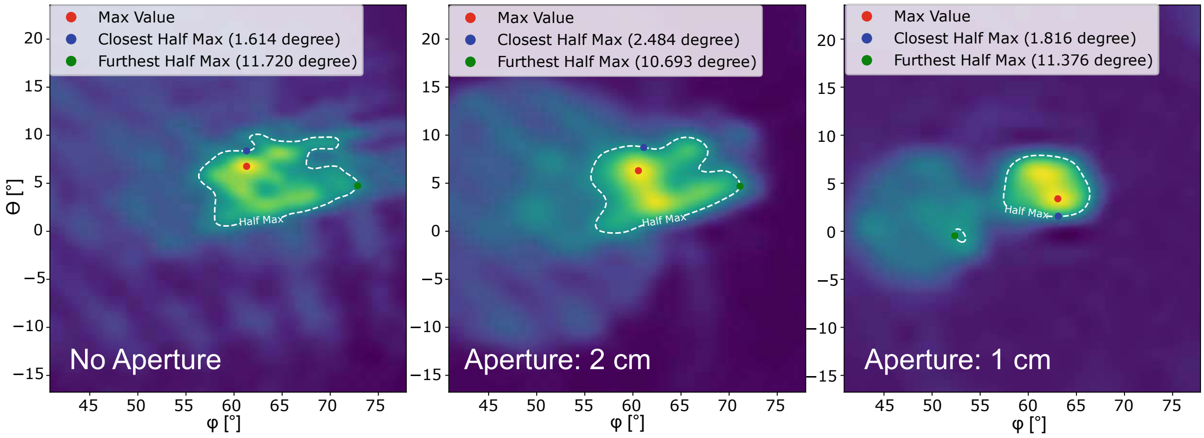

Figure 4.17: Far-field of Pan 17 measured at 9.5 cm at $\Theta = 0°$ with different apertures.

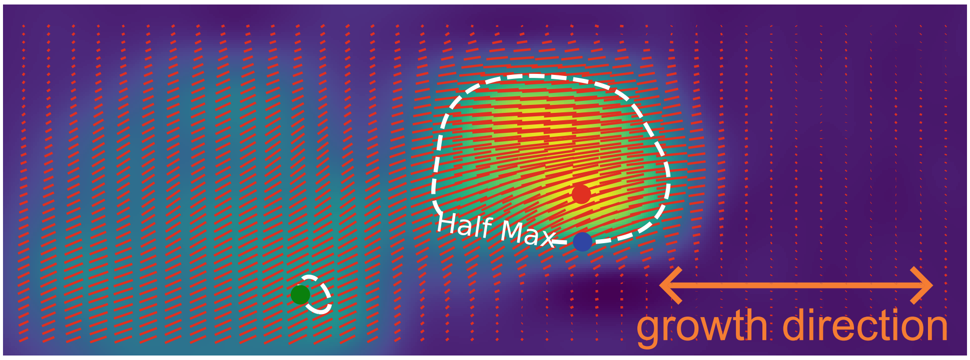

Figure 4.18: Far-field of Pan 17 measured at 9.5 cm at $\Theta = 0°$ with an aperture of 1 cm. The red lines indicate the polarization. Note that the device is placed inside the cryostat as shown in Figures 4.16 and 3.5, so the polarization of the main beam is aligned with the growth direction.

nearest half-maximum of less than 0.7 degrees (Figure 4.19), indicating a highly collimated beam. Figure 4.19b) not only shows a high-resolution zoom-in but also the measured polarization, which is perfectly aligned with the growth direction.

Egg 26

Device 26 shows two distinct maxima in the Θ direction and multiple very shallow ones in the φ direction, as illustrated in Figure 4.20. This same behavior can also be observed in other devices (Figures 4.17 and 4.19a). By increasing the distance and moving the aperture slightly, it is possible to isolate a single maximum, resulting in a very collimated beam. This phenomenon is observed for both pan- and egg-shaped devices, as illustrated in Figure 4.20b). The minimum achievable FWHM is 0.583°, which is very similar to the minimum FWHM for the pan-shaped device 17.
Therefore, the multiple maxima are most likely due to an interference pattern caused by reflections from the bottom gold layer or the ring itself.

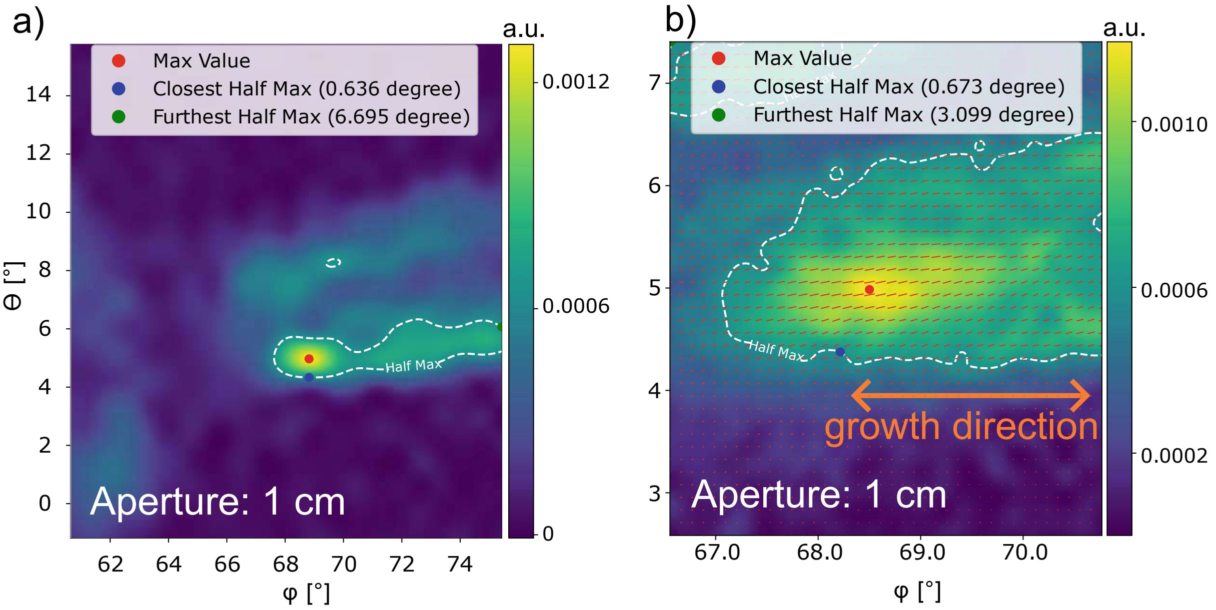

Figure 4.19: Far-field of Pan 17 measured at 9.5 cm at $\Theta = 0°$ with an aperture of 1 cm. The red lines indicate the polarization.

This is also supported by Figure 4.21, which shows the far-field of a perfect ring-shaped laser. Despite its symmetry, it exhibits noticeable interference patterns. Thus, the multiple maxima are not caused by the shape of the egg- and pan-shaped resonators.

Figure 4.22 shows the far-field of device 26 at different angles. Note the strong decrease in φ with increasing Θ. This circumstance is also illustrated in Figure 4.23 and will be further discussed in Section 4.4.6 .

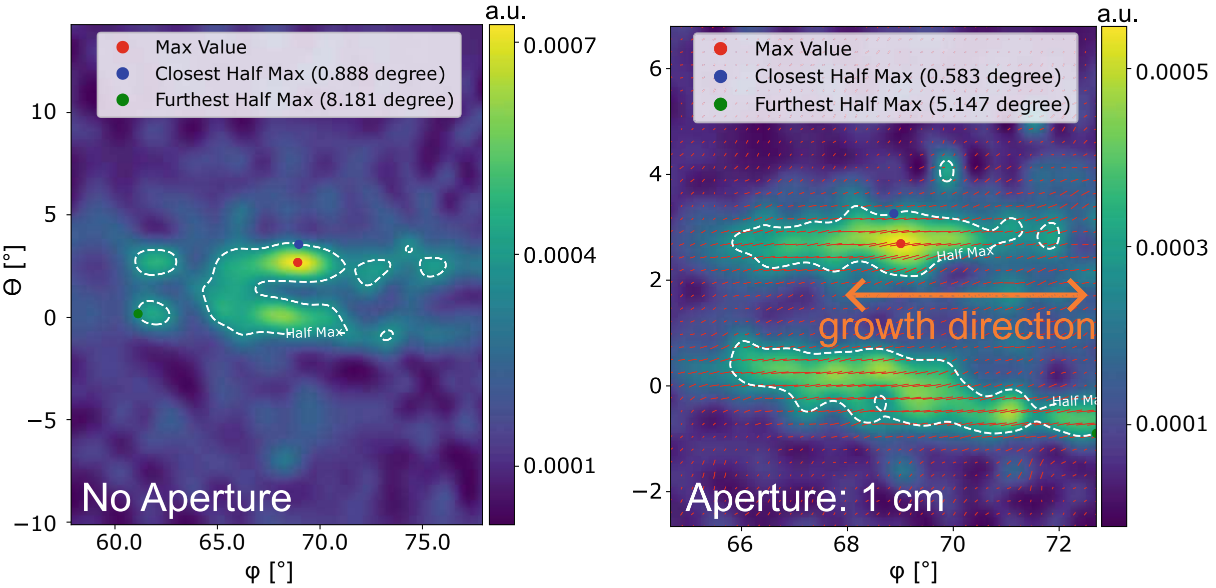

Figure 4.20: Far-field of device 26 measured at 22 cm with different apertures and resolutions.

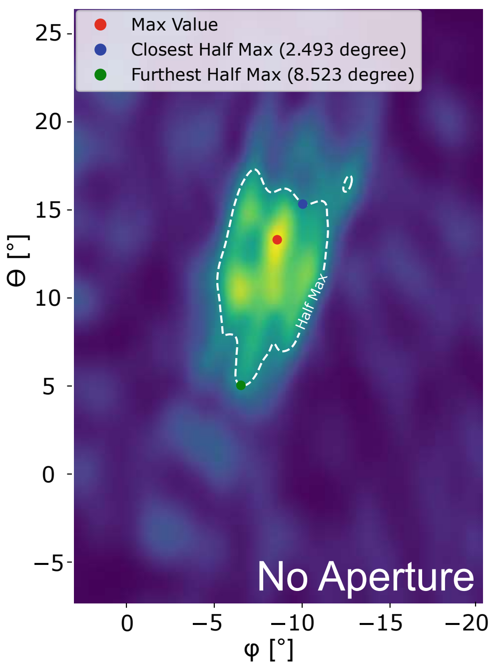

Figure 4.21: Far-field of a perfect ring-shaped laser at a distance of 9.5 cm.

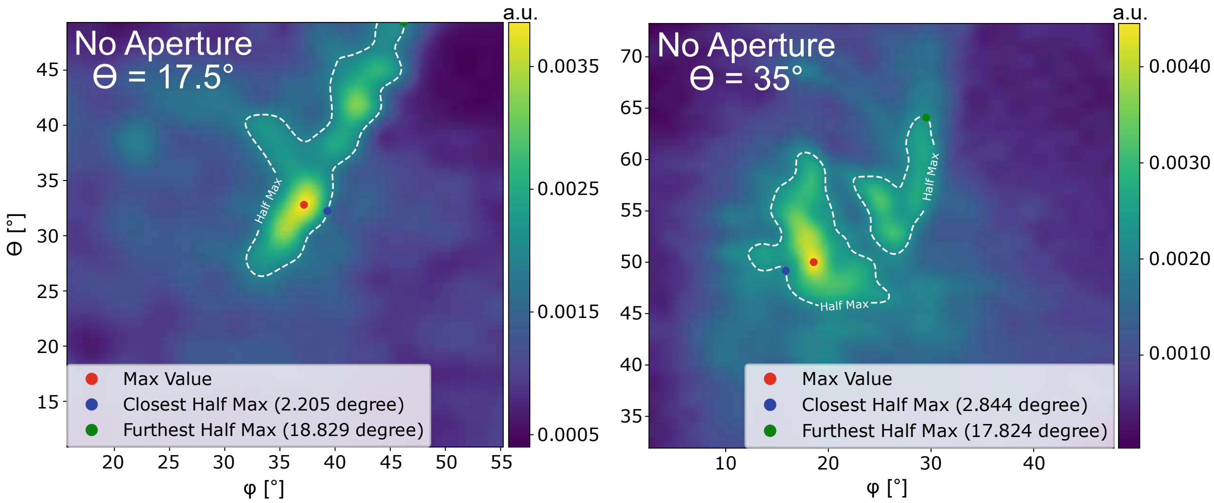

Figure 4.22: Far-field of device 26 measured at 22 cm at $\Theta = 17.5°$ and $\Theta = 35°$

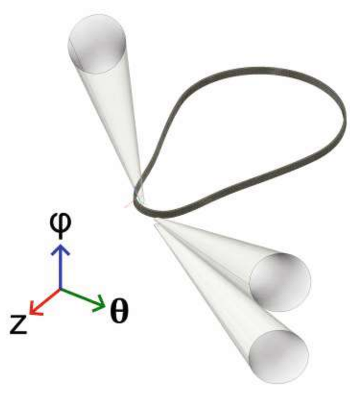

Figure 4.23: Direction of far-field radiation for different angles Θ, as shown in Figures 4.22 and 4.20. With increasing Θ, φ decreases drastically.

4.4.6 Statistical Trends

As not all measurements can be presented in detail, this section focuses on the statistical results across all measurements.

As mentioned in Section 4.4.5 and illustrated in Figure 4.23, there is a strong correlation between φ and Θ. Figure 4.24 provides an overview of the maximum far-field positions in terms of φ and Θ, where it is clearly visible that with increasing Θ, φ decreases significantly. Although the egg-shaped devices appear to radiate at lower Θ angles for the same φ angle, the difference is not statistically significant. The same applies for the influence of the minimum radius of the front section of the devices.

However, in terms of the minimum FWHM, egg- and pan-shaped devices differ significantly, as shown in Figure 4.25. The higher spread in beam width might be due to the multiple changes in curvature used for the pan-shape.

Figure 4.26 shows the minimum FWHM for different angles Θ. As can be observed, the beam width increases quite significantly with increasing Θ.
The minimum FWHM does also depend on the angle Θ, as Figure 4.26 shows. The beam width as well as the spread in beam width increases significantly with increasing Θ.

Figure 4.27 shows the position of the maximum of the far-field. The orange line connects the measurement points in decreasing size of the FWHM. Thus, the position of the far-field, especially in terms of the angle Θ, is positively correlated with the beam size. For increasing Θ, the beam width increases as well.

As presented in Figure 4.28, no dependence on the minimum radius or the design can be found, although simulations would imply different results. This might be due to the decreasing length of the arc section at smaller radii. Other reasons could be processing variations, reflections and interference, as well as differences in beam widths.

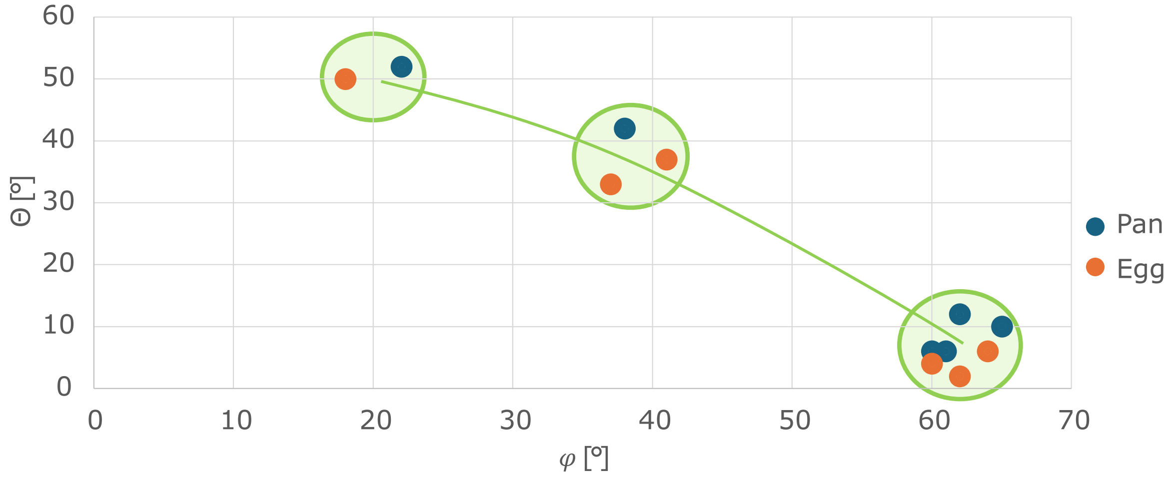

Figure 4.24: Position of the maximum far-field for all devices measured at a distance z of 9.5 cm.

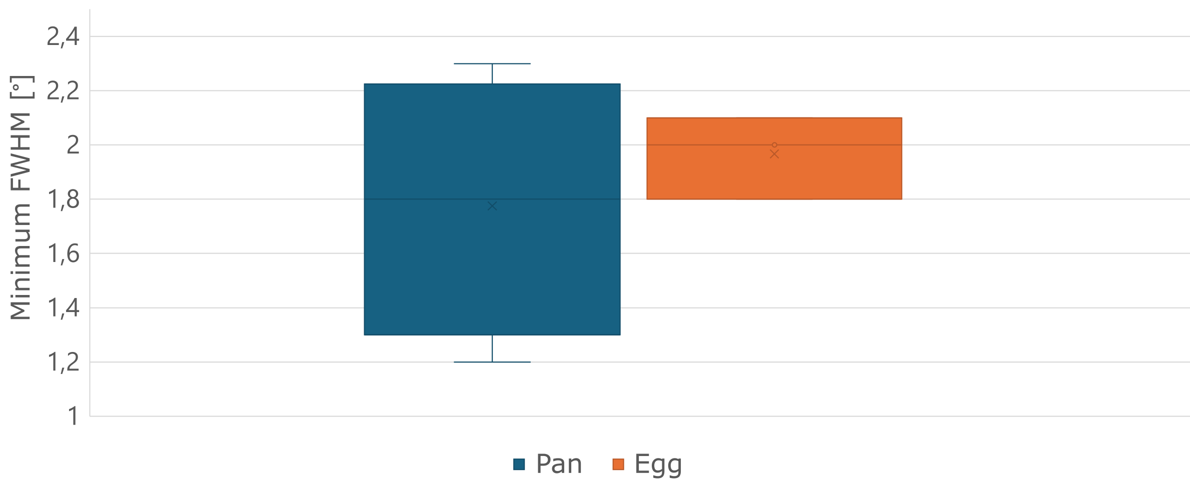

Figure 4.25: Comparison of the minimum FWHM of egg- and pan-shaped devices, measured at a distance z of 9.5 cm at $\Theta = 0°$.

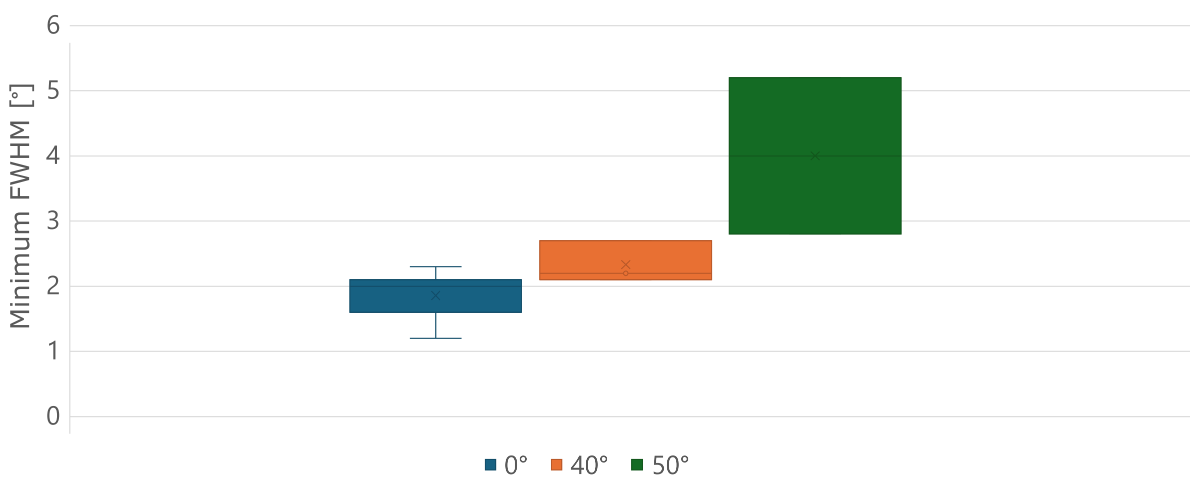

Figure 4.26: Comparison of the minimum FWHM of all devices for divergent angles Θ, measured at a distance z of 9.5 cm.

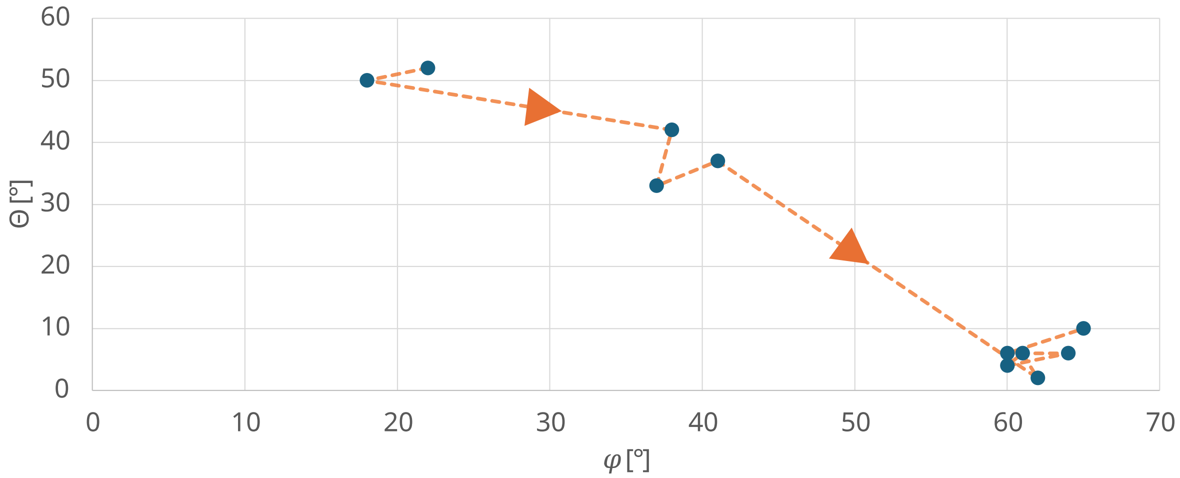

Figure 4.27: Position of the maximum of the far-field, measured at a distance z of 9.5 cm. The orange line connects the datapoints in the order of decreasing minimum FWHM.

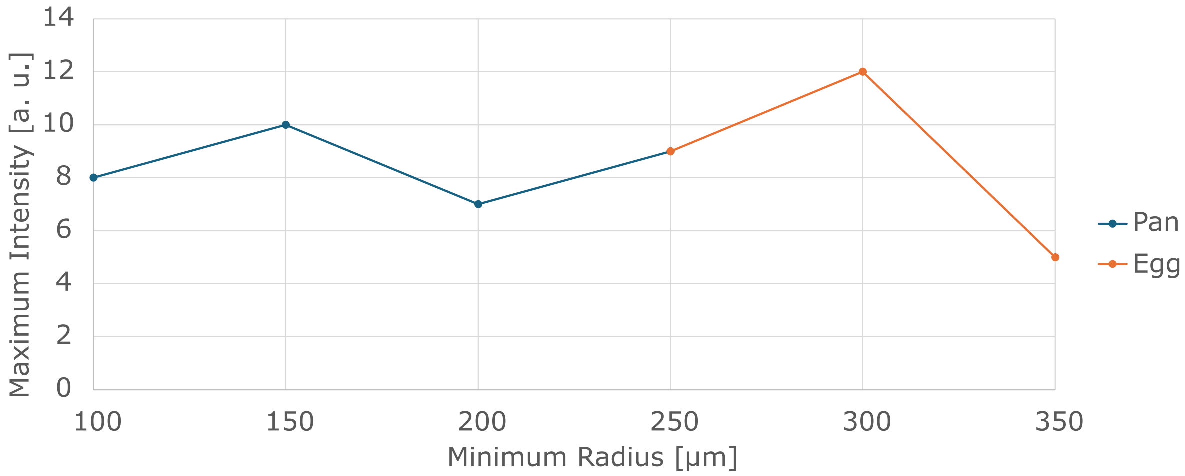

Figure 4.28: Maximum signal plotted in dependence of the minimum radius. Measured at a distance z of 9.5 cm at $\Theta = 0°$.

CHAPTER 5

Discussion and Outlook

Different novel resonator geometries were simulated and fabricated using nanofabrication techniques.

Two distinct geometries were tested: the so-called egg-shaped resonators, where two Euler bends connect two circular arc sections, and pan-shaped resonators, where four Euler bends connect two circular arc sections. The Euler bends provide a linear change in curvature, ensuring smooth transitions between different bend radii.
The pan-shaped resonators allow for an increased difference in radius between the front and back compared to egg-shaped devices, due to the inclusion of four Euler bends. However, the strong changes in curvature introduce side effects such as mode bouncing, leading to mode leakage.
In contrast, the egg-shaped resonators exhibit less pronounced changes in curvature. However, the achievable difference in radius is limited.

The devices showed two distinct operational modes: single-mode and multimode. In the case of multimode operation, an RF beatnote could be measured. By using an external RF generator, the laser could be injection-locked to the external signal, allowing the mode spacing to be modulated by up to 2 MHz.

The devices were also characterized in terms of their far-field emission, which was shown to be highly collimated. A minimum FWHM of less than 0.6 degrees was achieved with an egg-shaped device having a minimum radius of 350 μm.
The direction of radiation, due to the non-trivial geometry of the devices, is relatively complex. It was observed that the angle of radiation Θ increases with decreasing φ, reaching a maximum at $\varphi = 0°$.

The beam width was shown to decrease with decreasing angle Θ, and to be consequently smallest at an angle $\Theta = 0°$.

Although simulations indicated a strong dependence of the far-field emission on the minimum radius of the waveguide, this dependence could not be verified experimentally.

Despite extensive measurements, the characterization remains challenging. This is partly due to reflections and the limited size of the cryostat window, which restricts the measurable solid angle.
For improved characterization, a different measurement setup would be required. This setup would have to enable the measurement of a much larger solid angle while minimizing reflections and interferences.

Bibliography

[1] M. Jaidl *et al.*, "Comb operation in terahertz quantum cascade ring lasers", *Optica*, vol. 8, no. 6, pp. 780–787, Jun. 2021. DOI: 10.1364/OPTICA.420674.

[2] A. Leitenstorfer *et al.*, "The 2023 terahertz science and technology roadmap", *Journal of Physics D: Applied Physics*, vol. 56, no. 22, p. 223 001, 2023, Received 1 July 2022, revised 13 January 2023, accepted 23 February 2023, published 5 April 2023. DOI: 10.1088/1361-6463/acbe4c.

[3] A. Y. Pawar, D. D. Sonawane, K. B. Erande, and D. V. Derle, "Terahertz technology and its applications", *Drug Invention Today*, vol. 5, no. 2, pp. 157–163, 2013. DOI: 10.1016/j.dit.2013.03.009.

[4] M. Tonouchi, "Cutting-edge terahertz technology", *Nature Photonics*, vol. 1, pp. 97–105, Feb. 2007. DOI: 10.1038/nphoton.2007.3.

[5] R. A. Lewis, "A review of terahertz sources", *Journal of Physics D: Applied Physics*, vol. 47, no. 37, p. 374 001, 2014. DOI: 10.1088/0022-3727/47/37/374001.

[6] J. H. Booske *et al.*, "Vacuum electronic high power terahertz sources", *IEEE Transactions on Terahertz Science and Technology*, vol. 1, no. 1, pp. 54–75, 2011. DOI: 10.1109/TTHZ.2011.2151610.

[7] G. A. Komandin *et al.*, "BWO generators for terahertz dielectric measurements", *IEEE Transactions on Terahertz Science and Technology*, vol. 3, no. 4, pp. 440–444, 2013. DOI: 10.1109/TTHZ.2013.2255914.

[8] X. Li and J. Feng, "Microfabrication technologies for interaction circuits of THz vacuum electronic devices", *Micromachines*, vol. 15, no. 11, 2024. DOI: 10.3390/mi15111357.

[9] R. Lai *et al.*, "Sub 50 nm InP HEMT device with Fmax greater than 1 THz", in *2007 IEEE International Electron Devices Meeting*, Conference held December 10–12, 2007, IEEE, Washington, DC, USA, Dec. 2007, pp. 609–611. DOI: 10.1109/IEDM.2007.4419013.

[10] X. Mei *et al.*, "First demonstration of amplification at 1 THz using 25-nm InP high electron mobility transistor process", *IEEE Electron Device Letters*, vol. 36, no. 4, pp. 327–329, 2015. DOI: 10.1109/LED.2015.2407193.

[11] P. Smith *et al.*, "W-band high efficiency InP-based power HEMT with 600 GHz fmax", *IEEE Microwave and Guided Wave Letters*, vol. 5, no. 7, pp. 230–232, 1995. DOI: 10.1109/75.392284.

[12] W. Hafez and M. Feng, "Experimental demonstration of pseudomorphic heterojunction bipolar transistors with cutoff frequencies above", *Applied Physics Letters*, vol. 86, no. 15, p. 152 101, Apr. 2005. DOI: 10.1063/1.1897831.

[13] S. Khan *et al.*, "Terahertz radiation from high electron mobility avalanche transit time sources prospective for biomedical spectroscopy", *Photonics*, vol. 10, no. 7, 2023. DOI: 10.3390/photonics10070800.

[14] W. Kou *et al.*, "A review of terahertz sources based on planar schottky diodes", *Chinese Journal of Electronics*, vol. 31, no. 3, pp. 467–487, Mar. 2022. DOI: https://doi.org/10.1049/cje.2021.00.302.

[15] J. V. Siles, K. B. Cooper, C. Lee, R. H. Lin, G. Chattopadhyay, and I. Mehdi, "A new generation of room-temperature frequency-multiplied sources with up to 10× higher output power in the 160-GHz–1.6-THz range", *IEEE Transactions on Terahertz Science and Technology*, vol. 8, no. 6, pp. 596–604, 2018. DOI: 10.1109/TTHZ.2018.2876620.

[16] K. Kawase *et al.*, "Extremely high-intensity operation of a THz free-electron laser using an electron beam with a higher bunch charge", *Nuclear Instruments and Methods in Physics Research Section A: Accelerators, Spectrometers, Detectors and Associated Equipment*, vol. 960, p. 163 582, 2020. DOI: 10.1016/j.nima.2020.163582.

[17] G. P. Gallerano and S. Biedron, "Overview of terahertz radiation sources", in *Proceedings of the 2004 FEL Conference*, ENEA, UTS Advanced Physics Technologies, Frascati, Italy: JACoW, 2004, pp. 216–221.

[18] P. Chevalier *et al.*, "Widely tunable compact terahertz gas lasers", *Science*, vol. 366, no. 6467, pp. 856–860, 2019. DOI: 10.1126/science.aay8683.

[19] M. Tani, P. Gu, M. Hyodo, K. Sakai, and T. Hidaka, "Generation of coherent terahertz radiation by photomixing of dual-mode lasers", *Optical and Quantum Electronics*, vol. 32, no. 4, pp. 503–520, May 2000. DOI: 10.1023/A:1007070931314.

[20] M. Tani, O. Morikawa, S. Matsuura, and M. Hangyo, "Generation of terahertz radiation by photomixing with dual- and multiple-mode lasers", *Semiconductor Science and Technology*, vol. 20, no. 7, S151, Jun. 2005. DOI: 10.1088/0268-1242/20/7/005.

[21] D. Theiner, B. Limbacher, M. Jaidl, K. Unterrainer, and J. Darmo, "Flexible terahertz opto-electronic frequency comb light source tunable over 3.5 THz", *Opt. Lett.*, vol. 46, no. 22, pp. 5715–5718, Nov. 2021. DOI: 10.1364/OL.434974.

[22] K. A. McIntosh, E. R. Brown, K. B. Nichols, O. B. McMahon, W. F. DiNatale, and T. M. Lyszczarz, "Terahertz photomixing with diode lasers in low-temperature-grown GaAS", *Applied Physics Letters*, vol. 67, no. 26, pp. 3844–3846, Dec. 1995. DOI: 10.1063/1.115292.

[23] R. Kazarinov and R. Suris, "Possible amplification of electromagnetic waves in a semiconductor with a superlattice", *Soviet Physycs. Semiconductors*, vol. 5, pp. 707–709, Oct. 1971.

[24] R. Köhler *et al.*, "High-intensity interminiband terahertz emission from chirped superlattices", *Applied Physics Letters*, vol. 80, no. 11, pp. 1867–1869, Mar. 2002. DOI: 10.1063/1.1461054.

[25] R. Köhler *et al.*, "Terahertz semiconductor-heterostructure laser", *Nature*, vol. 417, no. 6885, pp. 156–159, May 2002. DOI: 10.1038/417156a.

[26] R. Sharma, H. Kaur, and M. Singh, "Recent advances of efficient design of terahertz quantum-cascade lasers", *Plasmonics*, vol. 16, no. 2, pp. 449–461, 2021. DOI: 10.1007/s11468-020-01295-4.

[27] L. Gao, C. Feng, and X. Zhao, "Recent developments in terahertz quantum cascade lasers for practical applications", *Nanotechnology Reviews*, vol. 12, no. 1, p. 20 230 115, 2023. DOI: doi:10.1515/ntrev-2023-0115.

[28] A. Khalatpour, M. C. Tam, S. J. Addamane, J. Reno, Z. Wasilewski, and Q. Hu, "Enhanced operating temperature in terahertz quantum cascade lasers based on direct phonon depopulation", *Applied Physics Letters*, vol. 122, no. 16, p. 161 101, Apr. 2023. DOI: 10.1063/5.0144705.

[29] P. Wang, K. K. Lee, G. Yao, Y. C. Chen, and R. G. Waters, "Carrier recombination rate in GaAS-AlGaAs single quantum well lasers under high levels of excitation", *Applied Physics Letters*, vol. 56, no. 21, pp. 2083–2085, May 1990. DOI: 10.1063/1.102979.

[30] F. H. Julien *et al.*, "Optical saturation of intersubband absorption in GaAs-AlxGa1-xAs quantum wells", *Applied Physics Letters*, vol. 53, no. 2, pp. 116–118, Jul. 1988. DOI: 10.1063/1.100386.

[31] Y. Arakawa, H. Sakaki, M. Nishioka, J. Yoshino, and T. Kamiya, "Recombination lifetime of carriers in GaAs-GaAlAs quantum wells near room temperature", *Applied Physics Letters*, vol. 46, pp. 519–521, Apr. 1985. DOI: 10.1063/1.95578.

[32] W. Huang *et al.*, "A unified figure of merit for interband and intersubband cascade devices", *Infrared Physics and Technology*, vol. 96, pp. 298–302, 2019. DOI: https://doi.org/10.1016/j.infrared.2018.11.033.

[33] B. S. Williams, "Terahertz quantum-cascade lasers", *Nature Photonics*, vol. 1, no. 9, pp. 517–525, 2007. DOI: 10.1038/nphoton.2007.166.

[34] F. Capasso *et al.*, "High-performance superlattice quantum cascade lasers", *IEEE Journal of Selected Topics in Quantum Electronics*, vol. 5, no. 3, pp. 792–807, 1999. DOI: 10.1109/2944.788453.

[35] H. Kaur, M. Singh, A. Chauhan, and R. Sharma, "Active region designs and mounting schemes of THz quantum-cascade laser", *Materials Today: Proceedings*, vol. 26, pp. 3458–3461, 2020, International Conference on functional materials and simulation techniques. DOI: https://doi.org/10.1016/j.matpr.2019.12.240.

[36] G. Scalari *et al.*, "Far-infrared (mu = 87 mum) bound-to-continuum quantum-cascade lasers operating up to 90 K", *Applied Physics Letters*, vol. 82, May 2003. DOI: 10.1063/1.1571653.

[37] S. Kumar and A. W. M. Lee, "Resonant-phonon terahertz quantum-cascade lasers and video-rate terahertz imaging", *IEEE Journal of Selected Topics in Quantum Electronics*, vol. 14, no. 2, pp. 333–344, Mar. 2008. DOI: 10.1109/JSTQE.2007.915510.

[38] V. Mitin, V. Kochelap, and M. A. Stroscio, *Quantum Heterostructures*. New York, NY: Cambridge University Press, Sep. 1999, Available in paperback.

[39] J. Faist, *Quantum Cascade Lasers*, English, Reprint. Oxford University Press, Mar. 2018.

[40] R. Paiella, *Intersubband Transitions in Quantum Structures*. New York, USA: McGraw-Hill Education Ltd, Apr. 2006.

[41] B. Williams, S. Kumar, H. Callebaut, Q. Hu, and J. Reno, "Terahertz quantum-cascade laser at $\lambda \approx 100\ \mu m$ using metal waveguide for mode confinement", *Applied Physics Letters*, vol. 83, pp. 2124–2126, Oct. 2003. DOI: 10.1063/1.1611642.

[42] K. Unterrainer *et al.*, "Quantum cascade lasers with double metal-semiconductor waveguide resonators", *Applied Physics Letters*, vol. 80, no. 17, pp. 3060–3062, Apr. 2002. DOI: 10.1063/1.1469657.

[43] M. A. Belkin *et al.*, “Terahertz quantum cascade lasers with copper metal-metal waveguides operating up to 178 K”, *Opt. Express*, vol. 16, no. 5, pp. 3242–3248, Mar. 2008. DOI: 10.1364/OE.16.003242.

[44] L. Rayleigh, “Cxii. the problem of the whispering gallery”, *The London, Edinburgh, and Dublin Philosophical Magazine and Journal of Science*, vol. 20, no. 120, pp. 1001–1004, 1910. DOI: 10.1080/14786441008636993.

[45] M. Jaidl *et al.*, “Silicon integrated terahertz quantum cascade ring laser frequency comb”, *Applied Physics Letters*, vol. 120, no. 9, p. 091 106, Mar. 2022. DOI: 10.1063/5.0078749.

[46] V. Braginsky, M. Gorodetsky, and V. Ilchenko, “Quality-factor and nonlinear properties of optical whispering-gallery modes”, *Physics Letters A*, vol. 137, no. 7, pp. 393–397, 1989. DOI: https://doi.org/10.1016/0375-9601(89)90912-2.

[47] M. Gorodetsky and A. Fomin, “Geometrical theory of whispering-gallery modes”, *IEEE Journal of Selected Topics in Quantum Electronics*, vol. 12, no. 1, pp. 33–39, 2006. DOI: 10.1109/JSTQE.2005.862954.

[48] D. G. Rabus and C. Sada, “Whispering gallery mode devices”, in *Integrated Ring Resonators: A Compendium*. Cham: Springer International Publishing, 2020, pp. 327–349. DOI: 10.1007/978-3-030-60131-7_7.

[49] D. Marcuse, “Bend loss of slab and fiber modes computed with diffraction theory”, *IEEE Journal of Quantum Electronics*, vol. 29, no. 12, pp. 2957–2961, 1993. DOI: 10.1109/3.259412.

[50] N. LORD, “Euler, the clothoid and $\int_0^\infty \frac{\sin x}{x} dx$”, *The Mathematical Gazette*, vol. 100, no. 548, pp. 266–273, 2016.

[51] F. Vogelbacher, S. Nevlacsil, M. Sagmeister, J. Kraft, K. Unterrainer, and R. Hainberger, “Analysis of silicon nitride partial euler waveguide bends”, *Opt. Express*, vol. 27, no. 22, pp. 31 394–31 406, Oct. 2019. DOI: 10.1364/OE.27.031394.

[52] D. Bachmann *et al.*, “Dispersion in a broadband terahertz quantum cascade laser”, *Applied Physics Letters*, vol. 109, no. 22, p. 221 107, Dec. 2016. DOI: 10.1063/1.4969065.

[53] P. Harrison and A. Valavanis, *Quantum Wells, Wires and Dots: Theoretical and Computational Physics of Semiconductor Nanostructures*, 4th. Wiley, 2016. DOI: 10.1002/0470010827.

[54] G. A. Reider, *Photonik: Eine Einführung in die Grundlagen*, 4th ed. Berlin, Germany: Springer-Verlag GmbH Deutschland, ein Teil von Springer Nature, 2022. DOI: 10.1007/978-3-662-62163-9.

[55] COMSOL, *RF Module User's Guide*, Version: COMSOL 5.5, COMSOL AB, Stockholm, Sweden, 2019.

[56] R. S. Elliott, "The farfield integrals, reciprocity, directivity", in *Antenna Theory & Design*. 2003, pp. 3–57. DOI: 10.1109/9780470544174.ch1.

[57] J. A. Stratton and L. J. Chu, "Diffraction theory of electromagnetic waves", *Phys. Rev.*, vol. 56, pp. 99–107, 1 Jul. 1939. DOI: 10.1103/PhysRev.56.99.

[58] T. Udem, R. Holzwarth, and T. Hänsch, "Femtosecond optical frequency combs", *The European Physical Journal Special Topics*, vol. 172, no. 1, pp. 69–79, 2009. DOI: 10.1140/epjst/e2009-01042-6.

[59] T. Udem, R. Holzwarth, and T. Hänsch, "Femtosecond optical frequency combs", *The European Physical Journal Special Topics*, vol. 172, no. 1, pp. 69–79, Jun. 2009. DOI: 10.1140/epjst/e2009-01042-6.

[60] J. Faist *et al.*, "Quantum cascade laser frequency combs", *Nanophotonics*, vol. 5, no. 2, pp. 272–291, 2016. DOI: doi:10.1515/nanoph-2016-0015.

[61] M. Roy, T. Zeng, and D. Burghoff, "Self-frequency-modulated laser combs", *Applied Physics Letters*, vol. 125, no. 7, p. 070 503, Aug. 2024. DOI: 10.1063/5.0215583.

[62] S. T. Cundiff and J. Ye, "Colloquium: Femtosecond optical frequency combs", *Rev. Mod. Phys.*, vol. 75, pp. 325–342, 1 Mar. 2003. DOI: 10.1103/RevModPhys.75.325.

[63] D. Burghoff *et al.*, "Terahertz laser frequency combs", *Nature Photonics*, vol. 8, no. 6, pp. 462–467, Jun. 2014. DOI: 10.1038/nphoton.2014.85.

[64] P. Friedli *et al.*, "Four-wave mixing in a quantum cascade laser amplifier", *Applied Physics Letters*, vol. 102, no. 22, p. 222 104, Jun. 2013. DOI: 10.1063/1.4807662.

[65] P. Gellie *et al.*, "Injection-locking of terahertz quantum cascade lasers up to 35GHz using RF amplitude modulation", *Opt. Express*, vol. 18, no. 20, pp. 20 799–20 816, Sep. 2010. DOI: 10.1364/OE.18.020799.

[66] A. Forrer *et al.*, "Photon-driven broadband emission and frequency comb RF injection locking in THz quantum cascade lasers", *ACS Photonics*, vol. 7, no. 3, pp. 784–791, Mar. 18, 2020. DOI: 10.1021/acsphotonics.9b01629.

[67] A. Forrer, L. Bosco, M. Beck, J. Faist, and G. Scalari, "RF injection of THz qcl combs at 80 K emitting over 700 GHz spectral bandwidth", *Photonics*, vol. 7, no. 1, 2020. DOI: 10.3390/photonics7010009.

List of Figures

1.1 Wien's Displacement Law . . . 9
1.2 Black Body Spectrum . . . 9

2.1 Comparison of interband and intersubband transition . . . 13
2.2 Illustration of the band diagram of two periods of a bound-to-continuum design of the active region of a QCL under bias voltage. . . . 14
2.3 Comparison of the absolute value of the electric field of mode profile of a double-metal ring laser with a height of 13 μm and a width of 45 μm at 2.4 THz. The top of the waveguide as well as the bottom plane are assumed to be ideal electrical conductors, and the GaAs laser is surrounded by vacuum. . . . 22
2.4 Radiated power coefficient of a ring laser at 2.4 THz with a height of 13 μm and different widths plotted over the outer radius of the ring. The solid lines represent the calculated values, while the lines with circular markers represent the simulated ones. . . . 23
2.5 Radiated power coefficient of a ring laser at 2.4 THz with a height of 13 μm and an outer radius of 1000 μm, considering material dispersion as defined in Equation 2.45, plotted as a function of the ring width. . . . 24
2.6 Euler spiral with $R_c = 1$ and $s_0 = 1$ . . . 25
2.7 Dielectric function according to equation (2.45) for GaAs . . . 26
2.8 In the frequency domain (a) the modes are equally spaced with the repetition rate f_{rep} and the distance from the first (virtual) mode to the origin f_{ceo}. In the case of AM, the laser emits pulses with a time separation equal to the inverse of the repetition rate of the laser in the time domain b). . . . 29
2.9 Principle of degenerate four-wave mixing (FWM) . . . 30

3.1 Screenshot of the geometry of a typical simulation with the waveguide (blue) in the center of the far-field domain. 33
3.2 Mounted and wire bonded sample with five lasers 34
3.3 Illustration of the processing of a double-metal ring laser. 35
3.4 Illustration of the measurement setup including the RF cable for RF injection and measurement. 36
3.5 Setup for measuring the far-field including the coordinate system in polar coordinates. A wire grid polarizer can be placed between the laser and the sensor to measure the polarization of the far-field (not shown). 37
3.6 Coordinate system in terms of θ and φ used for all far-field measurements, with the device placed vertically inside the cryostat. 38
3.7 Illustration of the alignment setup for determining an accurate zero position 38
3.8 Custom-built submount that enables tilting the laser in the Θ direction. The already mounted and connected QCL is rotated to $\Theta = 25$ degree. . 39

4.1 Comparison between egg-shaped resonators (a) and pan-shaped resonators (b). 42
4.2 Energy density of the mode in a device with four Euler bends showing very strong mode bouncing. 42
4.3 Far-field simulation of device 17 43
4.4 Simulation of the electric field in z direction of device 17 43
4.5 Simulated GVD for multiple waveguide widths with an outer radius of 1200 μm, considering material dispersion as defined in Equation 2.45. . . 44
4.6 Mask used for the optical lithography consisting of 10 different devices, numbered according to Table 4.1 and Table 4.2. The processed sample is cleaved horizontally between the devices. The rows are therefore denoted as a, b, and c, which are individually mounted onto a PCB. The value inside each device denotes the minimum radius in μm. 45
4.7 LIV of device 18 measured at 5 K and a duty cycle of 5 %. The dashed line represents the light measured with the lock-in amplifier, while the solid line shows the voltage measured on the PCB. 47
4.8 Spectrum of device 18 measured at 10 K in cw operation, showing three modes and multi-mode operation. For the multi-mode operation, a beat note was present (Figure 4.10). 47
4.9 Mode spacing of device 18 in the presence of a beat note, measured at 10 K in cw operation. 48
4.10 Electrical beat note of device 18 measured in cw operation. The bandwidth of the beat note is resolution limited to 51 kHz. 48

4.11 LIV of device 22 measured at 5 K and a duty cycle of 5%. The dashed line represents the light measured with the lock-in amplifier, while the solid line shows the voltage measured on the PCB. The red lines represent the measurement points in Figure 4.12. 49
4.12 Spectrum of device 22 operating in single-mode and multi-mode. Measured at 10 K in cw operation. 50
4.13 Spectrum of device 19 operating in multi-mode, measured at 10 K in cw operation. The three spectra correspond to the three beat note measurements shown in Figure. 51
4.14 Beat note of device 19 measured in cw operation, corresponding to Figure 4.13. The dots represent the measurement points, while the solid line is an interpolation. The orange beat note in the middle represents the free-running comb with no injection and a center frequency of 12.888635 GHz. The green and blue beat notes on the left and right are measured with RF injection. For the green beat note, an injection frequency of 6.44379 GHz is used, and for the blue one, 6.44491 GHz. The bandwidth of the beat note signals is resolution-limited to 68 kHz. A maximum pulling of about 2 kHz can be achieved. 51
4.15 Simulation of the change in a circular beam after reflecting off the cylindrical window flange of the cryostat compared to a measured reflection. As shown, not only does the shape change, but the polarization is also altered, as indicated by the red lines in the far-field pattern. Note that the device was mounted horizontally and not vertically as for the other measurements, consequently the polarization is perpendicular to the growth direction. . 53
4.16 Mounted sample inside the cryostat. The cylindrical window flange can be covered with THz-absorbing foil (not shown) to mitigate reflections. . . . 53
4.17 Far-field of Pan 17 measured at 9.5 cm at $\Theta = 0°$ with different apertures. 54
4.18 Far-field of Pan 17 measured at 9.5 cm at $\Theta = 0°$ with an aperture of 1 cm. The red lines indicate the polarization. Note that the device is placed inside the cryostat as shown in Figures 4.16 and 3.5, so the polarization of the main beam is aligned with the growth direction. 54
4.19 Far-field of Pan 17 measured at 9.5 cm at $\Theta = 0°$ with an aperture of 1 cm. The red lines indicate the polarization. 55
4.20 Far-field of device 26 measured at 22 cm with different apertures and resolutions. 55
4.21 Far-field of a perfect ring-shaped laser at a distance of 9.5 cm. 56
4.22 Far-field of device 26 measured at 22 cm at $\Theta = 17.5°$ and $\Theta = 35°$ . . . 56
4.23 Direction of far-field radiation for different angles Θ, as shown in Figures 4.22 and 4.20. With increasing Θ, φ decreases drastically. 56

4.24 Position of the maximum far-field for all devices measured at a distance z of 9.5 cm. 58
4.25 Comparison of the minimum FWHM of egg- and pan-shaped devices, measured at a distance z of 9.5 cm at $\Theta = 0°$. 58
4.26 Comparison of the minimum FWHM of all devices for divergent angles Θ, measured at a distance z of 9.5 cm. 58
4.27 Position of the maximum of the far-field, measured at a distance z of 9.5 cm. The orange line connects the datapoints in the order of decreasing minimum FWHM. 59
4.28 Maximum signal plotted in dependence of the minimum radius. Measured at a distance z of 9.5 cm at $\Theta = 0°$. 59

List of Tables

4.1 Parameters for waveguide designs with 2 Euler bends 43
4.2 Parameters for waveguide designs with 4 Euler bends 43
4.3 Threshold current density and maximum current density at a heat sink temperature of 5 K and a duty cycle of 5 % for different devices. Sample a, b, and c denoted according to Figure 4.6. 46